Raman Spectroscopic Properties of Aqueous Chloride Salt Solutions: Chlorides of Alkalis, Alkaline Earths and First-Row Transition Metals

By

Spencer Poulette

A thesis submitted in partial fulfillment of the requirements of the degree of

Master of Science

Department of Earth and Atmospheric Sciences

University of Alberta

Abstract

Saline aqueous fluids play numerous key roles in many geologic processes, but how fluids flow and interact with rocks depends on their physical and chemical properties, which in turn depend on the types, concentrations, and speciation of solutes. Raman spectroscopy is a powerful tool to identify and characterize solutes in geologic fluids, for example by analysis of fluid inclusions in minerals, but our knowledge and understanding of the Raman spectroscopic properties of aqueous solutes is still limited. Here, we present a survey of the Raman spectroscopic properties of aqueous salt solutions at ambient temperature and pressure and over wide ranges of fluid composition, with a focus on chloride salts. Specifically, we analyzed solutions ranging from pure H_2O up to salt saturation for 19 different chloride salts, mostly from group 1 (alkalis), group 2 (alkaline Earths), and the first-row transition metals. For each salt, we evaluated how increasing the concentration affects the Raman spectroscopic properties of the solvent H_2O; and for many of the salts we also identify the characteristic Raman peaks that are distinct from those of H_2O and thus reveal the formation of metal-ligand complexes in solution. Broadly, we find that the studied salts can be divided into two main categories: those that distort the OH-stretching region of the H_2O spectrum but do not show evidence of ion pair formation; and those that show the emergence of new Raman peaks with increasing concentration indicative of ion pair formation. We find that the decisive factor that differentiates these two categories seems to be the ionic radius of the cation, with ion pair formation enabled when the ionic radius of the cation is less than about 100 pm. Moreover, we find that especially amongst the salts that do not show evidence for ion pair formation, the distortion of the OH-stretching band generally conforms to a remarkably simple relationship between Raman peak intensities and molal concentration of chloride. Our results thus allow for fast identification and quantification of some aqueous electrolyte solutes and species;

provide insight into their speciation; and allow for calibration of a Raman spectroscopic proxy measurement for fluid salinity, and potentially pH.

Preface

This thesis is to be submitted to GCA upon completion. I was responsible for data collection, conducting data analysis, and composing the manuscript. Matthew Steele-MacInnis supervised this study and contributed to revising the manuscript.

Acknowledgments

I would like to thank my supervisor, Matthew Steele-MacInnis for his continual support and patience in the course of writing this thesis. I would also like to thank my family and friends for their understanding and unending support of my endeavours. As well, a thanks to Opal and Onyx the axolotls who remind me to breathe, Iroh the pacman frog who reminds me to relax sometimes, and Sirona the ball python who reminds me to push my curiosity. This thesis would not have been possible without the support of everyone around me.

Table of Contents

List of Tables

List of Figures

1. INTRODUCTION

Aqueous fluids affect virtually all geologic processes from Earth's surface to Earth's deep interior, as well as in extraterrestrial settings. However, the physical and chemical properties of geologic fluids vary widely, which in some cases renders quantitative interpretation of these processes challenging. This wide variation in properties is in part because geologic fluids exhibit wide ranges of chemical composition involving numerous electrolyte and non-electrolyte solutes (Steele-MacInnis and Manning, 2020; Steele-MacInnis et al., 2021). Because different solutes interact differently with solvent H_2O (and each other), the identities of the solutes and their speciation at the molecular scale are critical to understanding the macroscopic properties of the fluid (Steele-MacInnis and Manning, 2020). For example, addition of electrolyte solutes has strong effects on the solubilities of minerals owing largely to the interactions between electrolytes and solvent, as well as via formation of complexes (Brooks and Steele-MacInnis, 2019); and electrolyte solutes also strongly affect phase equilibria and criticality of hydrothermal aqueous fluids (Klyukin et al., 2016). As such, analytical methods that probe molecular-scale properties and interactions in aqueous fluids are crucial to improving our understanding of geologic processes.

Raman spectroscopy is a relatively fast and accessible analytical technique that can provide a wealth of information on the identities, speciation and molecular environment of solutes in aqueous fluids. Over the past several decades, a significant amount of analytical work has been done in characterizing geologic fluids by Raman spectroscopy of fluid inclusions in minerals (e.g., Burke, 2001; Frezzotti et al., 2012; Bodnar and Frezzotti, 2020), as well as in various high-pressure optical cells to probe geologic fluids in situ during hydrothermal experiments (e.g., Lin et al. 2007; Chou, 2012; Schmidt and Chou, 2012; Reimer et al., 2015;

DeVitre et al., 2021). Many of these previous studies have focused on characterizing the Raman spectroscopic properties of saline aqueous fluids, with applications for example to estimating the salinity of aqueous fluid inclusions (Mernagh and Wilde, 1989; Baumgartner and Bakker 2009; Sun et al. 2010); identifying solutes, their aqueous speciation and solvation environment (e.g., Walter et al., 2018; Szmihelsky et al. 2021; Foustoukos, 2016; Scholten et al., 2019; Schmidt et al., 2018); and estimating fluid pH (Dubessy et al., 1992). However, at present one of the principal obstacles to such applications is a general lack of information on the characteristic Raman spectroscopic properties of numerous geologically relevant solutes and how they vary with concentration. For example, hydrothermal aqueous brines in a number of settings show concentrations of first-row transition metals ranging up to multiple weight-percent levels (Yardley, 2005; Bodnar et al., 2014), and these metal concentrations show clear positive correlation with chloride content (Yardley, 2005), but information regarding the Raman spectroscopic properties of many aqueous metal-chloride solutions remain scarce.

As a starting point for considering the effects of salinity on the Raman spectrum of aqueous fluids, it is appropriate to first outline the general Raman spectroscopic features of H_2O (Fig. 1). An intense Raman feature at low wavenumber (<100 cm^{-1}), denoted "translational region" in Fig. 1, has been interpreted to represent the effects of rotational shearing of individual H_2O molecules (Walrafen and Chu, 1995). A weak and relatively broad feature at ~1640 cm^{-1} corresponds to the H–O–H bending mode of H_2O molecules (Walrafen and Chu, 1995; Sun, 2009). Both of the latter regions are of limited application to interpreting the properties of salt solutions, and the main focus of most studies is on the O-H stretching region from ~3000 to 4000 cm^{-1}. The latter region is characterized by a broad and asymmetric band that is obviously composed of multiple overlapping peaks, but the exact number of peaks and their relationships to

vibrational modes is unclear and deeply controversial in the literature (Garcia-Baonza et al., 2012). Several papers have attempted to resolve the controversy of vibrational mode assignments by combining Raman and X-ray spectroscopic techniques (Walrafen and Chu, 1995; Khoshtariya et al, 2004; Steinbach et al, 2004; Sun, 2009). In addition, theoretical modelling and simulations have been performed by several authors on the structure of water and predicted Raman modes (e.g., Devendorf *et* al, 1996; Li *et al*, 2017; Senanayake *et al*, 2021), but because of computational limitations, only small clusters of water molecules have been successfully modelled, which limits the accuracy of these models in comparison to real fluids. Generally speaking, most studies agree that the most intense peak (centered at ~3380 cm-1) can be interpreted to represent "poorly connected" (weakly hydrogen bonded, with few neighbors) H_2O; whereas the large shoulder at ~3250 cm^{-1} represents "network" (hydrogen bonded) H_2O; and the small shoulder at ~3640 cm^{-1} represents free H_2O monomers (Brubach et al., 2005). That said, various interpretations of these peaks exist and these have also led to various approaches of how to quantitatively interpret the Raman spectrum with fitted peaks. Most studies that have focused salinity estimation in aqueous fluids use two or three peaks for their fits (Baumgartner and Bakker, 2009; Sun *et al,* 2010), whereas studies focusing on the molecular structure of water have generally used four or five peaks (Carey and Korenowski, 1998; Furic *et al*, 2000; Chumaevskii, 2001; Sun, 2009; Li *et al*, 2017).

Briefly, the addition of solutes to an aqueous fluid is expected to have two main types of effects on the Raman spectrum of the resulting solution. Firstly, various solute species may have their own characteristic vibrational modes that appear as specific Raman peaks (Frezzotti et al., 2012). For example, the aqueous sulfate ion (SO_4^{2-}) has a characteristic Raman peak at ~980 cm^{-1}) that has been used in several studies to identify sulfate-rich fluids in fluid inclusions (Frezzotti

et al., 2012; Walter et al., 2018; Szmihelsky et al., 2021). In the case of dissolved chloride salts, fully ionized solute species would generally not be expected to show Raman peaks (with the exception of the ammonium ion, which has its own internal vibrational modes), but bonded species such as ion pairs may have such peaks. Secondly, electrolyte solutes are known to strongly affect the structure of the solvent H_2O, for example disrupting hydrogen bonding and forming solvation shells around ions. As such, dissolved chloride salts are expected to have strong effects on the Raman peaks characteristic of H_2O. The latter effects have been confirmed and analyzed quantitatively in several studies, which all show a general tendency of decreasing the Raman intensity related to hydrogen bonded water, and increasing Raman intensity related to depolymerized H_2O molecules, with increasing salinity (Schultz and Hornig, 1961; Walrafen, 1962; Mernagh and Wilde 1989; Baumgartner and Bakker, 2009; Sun et al., 2010; Frezzotti et al., 2012).

Here, we present the results of a detailed survey of the Raman spectroscopic properties of aqueous chloride salt solutions at ambient pressure and temperature, and at concentrations ranging from dilute to saturated, for 19 chloride salts. The analyzed salts belong mostly to the alkalis (H through Cs), alkaline Earths (Mg through Ba), and first-row transition metals (Mn through Zn), along with ammonium and tin(II) chlorides. In the case of Fe, we also analyzed solutions of both common oxidation states, $FeCl_2$ and $FeCl_3$. Our data provide a comprehensive picture of how these diverse solutes affect the Raman spectroscopic properties of aqueous solutions, potentially allowing for straightforward estimation of fluid salinity (and in some cases, potentially also concentrations of specific metals, as well as pH) based on Raman analysis, and also allow us to uniquely identify various cation-chloride solutes and species according to their characteristic Raman peaks. Furthermore, our results provide some hints into the underlying root

causes, at the molecular scale, for why certain cations tend to form explicit chloride complexes whereas others do not. These results will serve as a foundation for quantitative interpretation of Raman spectra of saline aqueous fluids.

2. MATERIALS AND METHODS

We prepared solutions of known concentration by gravimetric analysis of 19 different chloride salts as outlined in Table 1. Solutions were prepared using MilliQ deionized water, a variety of crystalline reagents (or an aqueous stock solution in the case of HCl; all summarized in Table 1), and a Mettler Toledo ME104 high precision analytical balance. In most cases, we first prepared a stock solution of high concentration, which was subsequently diluted in aliquots to generate a range of concentrations. However, for some of the reactive solutes such as $FeCl_2$, we prepared fresh solutions for each increment of concentration, following the same procedures as outlined by Steele-MacInnis et al. (2015) and Lecumberri-Sanchez et al. (2015) to avoid oxidation of the solute.

After preparation of the solutions, aliquots were split for measurements of fluid density and Raman spectroscopy. Density measurements were collected for each solution using a Mettler Toledo Densito 30px handheld densitometer. We then performed multiple linear regression analysis to generate simple empirical equations that can be used to estimate solution density as a function of salinity for each solute (see Table 2). Note that the equations relating fluid density to salinity are necessary to express salinities in units of molarity (moles of solute per litre of solution), such as was done by Sun et al. (2010).

Raman spectra of the crystalline salts, pure H_2O, and the aqueous salt solutions were collected using a Horiba Scientific LabRam Evolution HR Raman spectrometer. Spectra were acquired using a 532 nm laser with a nominal power at the source of 100 mW. Crystalline salts were analyzed on a glass plate, whereas aqueous solutions were held in silica glass cuvettes mounted in a cuvette holder in the laser path (Fig. 2). The confocal aperture hole was opened to 400 μm. The Raman spectrum of the silica glass cuvette was also acquired by analyzing an empty cuvette using the same instrument settings. We used an 1800 grooves/mm grating for high spectral resolution and collected spectra across the full range of 50 to 4000 cm^{-1}. All spectra were collected for 30 seconds per acquisition (at each spectrometer position across the spectral range) for 3 accumulations each.

As discussed in more detail below, we experimented with peak fitting of the Raman data using the Fityk 1.1.2 and LabSpec6 software packages. Where necessary, we subtracted a linear baseline, and we attempted to fit the OH-stretching region using either a 2, 3 or 5-peak model as discussed above. However, ultimately, we found that the most self-consistent results were obtained by forgoing peak fitting, owing to the complex nature of the OH-stretching region that is composed of multiple, broad and overlapping Raman peaks. Therefore, the quantitative analysis of the effect of chloride concentration on the OH-stretching region discussed below (Section 4.3) does not involve peak fitting and was instead developed using only the relative intensities at specific Raman shifts.

3. RESULTS

3.1 Density

All aqueous chloride salt solutions studied here show an expected trend of increasing fluid density with increasing salinity (Fig. 3), but the relationship between fluid density and salinity differs between individual salts. For the alkalis, the variation in density with solute type can be easily rationalized in terms of increasing molecular mass of the solutes, with density at any given salinity increasing in the same order as atomic number of the cation, thus H < Li < Na < K < Rb < Cs (Fig. 3A). In contrast, no such straightforward relationship is evident for the alkaline earths and first-row transition metals (Fig. 3B and C), likely reflecting the competing influences of molecular masses, ionic radii of the cations (which affect field strength and hence degree of electrostriction, or volumetric collapse, of the solvent), and complexing reactions in solution that may yield a variety of both charged and neutral species.

3.2 Raman Spectra

3.2.1 Alkalis

None of the crystalline alkali chloride salts analyzed here showed any obvious Raman peaks (lowermost spectra on each panel of Fig 4), and in general most of the alkali chlorides (specifically, NaCl, KCl, RbCl and CsCl) showed no unique Raman peaks in solution and showed similar effects on the O-H stretching region. Regarding NaCl and KCl, this was expected as these had been previously characterized by Sun et al. (2010), and our results mostly corroborate and add detail to the latter results. In the case of RbCl, the similar ionic radius of Rb^+ to K^+ suggests that similar Raman response would be expected, and indeed we find that this is

the case. Addition of all four of the latter alkali chlorides generally causes a decrease in the intensity of the Raman region corresponding to hydrogen-bonded water, and an increase in the intensity related to weakly hydrogen bonded and free H_2O (Fig. 4). Two of the alkali chlorides—namely, HCl and LiCl—show somewhat different results compared to the others and are discussed separately below.

In the case of LiCl, we observe the appearance of an additional, new Raman peak at 370 cm^{-1}, which becomes evident above ~5 wt% LiCl and shows increasing intensity with increasing concentration of LiCl (Fig. 4). The peak is broad and relatively weak even when concentration is high, and also overlaps partly with a Raman peak that corresponds to the silica-glass cuvette, but nevertheless the increasing intensity of this peak with increasing LiCl content makes the assignment of this peak to an aqueous species unique to LiCl solutions reasonably confident. The HCl solutions, in contrast, show no obvious new peaks at low wavenumber but instead show the emergence of a strong, broad peak centered at ~2800 cm^{-1} and strongly overlapping with the low-wavenumber part of the O-H stretching band (Fig. 4). The intensity of this peak increases strongly with increasing HCl concentration, and the interpretation and application of this peak are discussed further below (Section 4.3.2).

3.2.2 Alkaline Earths

All four of the alkaline earth chlorides studied here were added to solution in the form of salt hydrates, and consequently the Raman spectra of the crystalline compounds mostly show characteristic Raman spectra in the O-H stretching region, reflecting vibrational modes of H_2O in each crystal structure (Fig. 5). In their aqueous solutions, the alkaline earth chlorides generally

follow similar trends compared to the alkalis, showing a relative increase in the intensity of the weakly hydrogen bonded H_2O and a concomitant drop in the intensity of the hydrogen-bonded water, as concentration of each salt is increased (Fig. 5). Chlorides of Ca, Sr and Ba do not show the emergence of any additional peaks, and the only exception to this observation amongst the alkalis is $MgCl_2$, which shows a broad, weak peak emerge at ~356 cm^{-1} at concentrations greater than ~8 wt%.

3.2.3 First Row Transition Metals

The Raman spectrum of $MnCl_2 \cdot 4H_2O$ does not show any distinct peaks of H_2O, owing to luminescence at high wavenumber (Fig. 6A). Raman spectra of $FeCl_2 \cdot 4H_2O$ and $NiCl_2 \cdot 6H_2O$ display characteristic vibrational modes of H_2O within the crystal structure of the crystalline compounds (Fig. 6B, E). In addition, these compounds show Raman peaks at low wavenumber, which are not coincident with the peaks observed in the corresponding aqueous solutions discussed below. Both $CoCl_2 \cdot 6H_2O$ and $ZnCl_2$ show Raman peaks at low wavenumber, which again are not coincident with the Raman peaks observed in the aqueous solutions of these salts (Fig. 6D, G). Anhydrous ferric chloride ($FeCl_3$) also shows Raman peaks at low wavenumber, one of which is coincident with the main peak seen in the aqueous solutions of $FeCl_3$ at 318 cm^{-1} (Fig. 6C). Copper(II) chloride ($CuCl_2$) shows no obvious Raman peaks at low wavenumber, and although we analyzed nominally anhydrous CuCl2 we observe a Raman signal in the OH-stretching region (Fig. 6F) which likely reflects adsorption of H_2O due to exposure to air during the analysis.

Aqueous solutions of $MnCl_2$ and $FeCl_2$ show similar trends compared to the alkali and alkaline-earth salts described above, with regard to the modification of the OH-stretching region with increasing salinity. In contrast, the other first row transition metal chloride salts (of Co, Ni, Cu and Zn) do not show the same trends in modification of the OH-stretching region with increasing salinity as seen in the alkalis and alkaline Earth metal chlorides, and instead show only subdued depression of the Raman intensity interpreted to reflect hydrogen-bonded H_2O, coupled with overall weakening of the Raman intensity of the OH-stretching region. Consequently, and as discussed in more detail below (section 4.3.1), these latter salts do not conform to the same calibration equation to estimate salinity based on Raman spectra over the whole range of concentrations studied here. Chloride salt solutions from this group also show additional peaks appearing between 200 and 400 cm^{-1} in their Raman spectra which are discussed below (Fig. 6).

Raman spectra of $MnCl_2$ solutions show an additional peak at ~355 cm^{-1} that becomes evident at >10 wt%. This peak is broad and weak compared to the rest of the spectrum, similar to those of $MgCl_2$ and LiCl (Fig. 6A). Spectra of $FeCl_2$ solutions also show an additional broad, weak peak at ~368 cm^{-1} which becomes distinguishable from the background at >15 wt% (Fig. 6B). The $FeCl_3$ solutions show an additional peak at ~318 cm^{-1}, which is evident even at concentrations <5 wt% (Fig. 6C). The peak morphology of this latter peak is sharp and narrow, and is clearly distinct from the ~368 cm^{-1} peak observed in the $FeCl_2$ solutions.

Solutions of $CoCl_2$ show an additional broad band centred at ~255 cm^{-1} that seems to be composed of multiple, overlapping peaks (Fig. 6D). This feature becomes visible at >10 wt%. The $NiCl_2$ solutions show an additional sharp peak at ~390 cm^{-1} at concentrations >10 wt% (Fig. 6E). Solutions of $CuCl_2$ show a peak centred at ~287 cm^{-1} that becomes evident at >5 wt% (Fig.

6F). Solutions of $ZnCl_2$ show an additional peak at ~294 cm^{-1} at concentrations >10 wt%. At higher concentrations (>70 wt%), another new peak emerges at ~242 cm^{-1} (Fig. 6G). Both of these latter peaks are sharp and narrow. An additional peak also occurs in solutions of high $ZnCl_2$ concentration (>70 wt%) at 3500 cm^{-1}. However, the concentrated solutions of $ZnCl_2$ of >20 wt% also show strong luminescence at high wavenumber, which for example renders the weak OH-bending mode unresolvable.

3.2.4 Tin(II) and ammonium

The studied $SnCl_2$ solutions show the emergence of two additional Raman peaks at 220 and 270 cm^{-1} as concentration increases. The 270 cm^{-1} peak becomes evident above ~3 wt% $SnCl_2$, whilst the 220 cm^{-1} peak only becomes evident at concentrations >20 wt% $SnCl_2$. These solutions also showed a broad peak at 2800 cm^{-1}, the same as observed in the HCl solutions, and this reflects the fact that the $SnCl_2$ solutions used here contained a known, finite concentration of HCl that was added to help solubilize the $SnCl_2$.

The studied NH_4Cl solutions showed several additional peaks centred at ~1435, ~1700, ~2885, and ~3070 cm^{-1}, all of which correspond to the known, internal vibrational modes of the ammonium ion (Krishnan, 1947). As expected for such internal modes, these peaks are evident in all solutions of >1 wt% NH_4Cl, and the relative intensities of the four peaks remain approximately the same independently of concentration whereas the absolute intensities of all four peaks increase compared to the O-H stretching band of the solvent as the ammonium concentration increases. The shape of the O-H stretching band meanwhile follows approximately

the same trend with increasing salinity as compared to the alkalis, as expected considering the geochemical similarity of ammonium to potassium.

4. DISCUSSION

4.1 Density

The density data can be transformed into calculated molar volume of each solution, which when plotted as a function of concentration in molar fraction allows for evaluation of partial- and apparent-molar volumes, as well as qualitative assessment of the degree of (non)ideality of mixing between solute and H_2O (Figures 7-9). Most of the chloride solutions show molar volumes trended below the ideal mixing line in these plots, especially at low concentrations (Figures 7-9), which generally reflects ionization of the solutes and hence electrostriction of the solvent H_2O. Such "better than ideal" mixing behaviour is exhibited for example by solutes that are known to mostly ionize even at high concentration, such as NaCl and $CaCl_2$; but is also seen for salts that likely form charged complexes such as $FeCl_3$. In contrast, several of the salts (HCl, RbCl, $SrCl_2$, CsCl, and $BaCl_2$) show trends towards nearly ideal mixing as salinity increases. In the case of HCl, this mixing trend probably reflects formation of neutral ion pairs that do not strongly attract H_2O; whereas in the case of large cations like Sr, Ba and Cs it likely reflects only weak electrostriction owing to the relatively low field strength of the cation. Only a few salts—most prominently $FeCl_2$—show solution molar volumes clearly exceeding that of an ideal mixture, which may reflect for example, formation of explicitly hydrated complexes in which the particle density of H_2O units is lower than that of the surrounding solvent.

4.2 Aqueous Complexes

4.2.1 Interpretation of Raman Spectra

Our results show no evidence of specific Raman peaks for most of the alkali or alkaline-earth chlorides—the key exceptions being HCl, LiCl and $MgCl_2$—whereas in contrast our results show clear evidence of characteristic Raman peaks for all of the studied transition metal chlorides as well as $SnCl_2$ (Table 1). In the case of ammonium chloride, the known internal modes of the tetrahedral NH_4^+ ion are evident but are not indicative of complex formation, and indeed the general trends of how ammonium chloride influences the Raman spectrum of the aqueous solution are essentially the same as for that of potassium chloride, as expected owing to the same charge and similar ionic radii of ammonium and potassium. That being said, the characteristic Raman peaks listed in Table 1 can be used as a guide during spectroscopic analysis, for example of fluid inclusions in minerals, to identify key solutes. Here, we briefly discuss the specific, characteristic peaks of each of the solutes that show evidence of complex formation and attempt where possible to relate them to aqueous species.

Hydrogen chloride is unique amongst the solutes considered here in that it shows the emergence of a Raman peak at high wavenumber (~2800 cm^{-1}), overlapping partly with the O-H stretching region of the solvent (Fig. 1C). In light of this overlap with the O-H stretching region, it might be reasonable to interpret this peak as representing hydronium-type complexes (e.g., H_3O^+ or some more polymerized variant) in these highly acidic solutions, and indeed this Raman peak was interpreted as such by Busing and Horig (1961) and Walrafen (1962). However, this peak also appears in the Raman spectrum pure gaseous HCl (Salant and Sandow, 1931) as well as in HCl-Ar gas mixtures (Devendorf *et al*, 1996), wherein hydronium-type complexes obviously cannot be formed. Hence, it appears that this peak corresponds to the stretching

vibration of H-Cl complexes—an interpretation consistent also with results of molecular simulations of HCl in the gas phase (Grayson, 2003). This peak, which has also been observed in acidic, metal-rich hydrothermal fluids (Schmidt, 2018), shows increasing intensity with increasing concentration of HCl, and below we discuss its potential use as a spectroscopic proxy for estimating HCl content and, hence, pH.

The only other alkali chloride to show the emergence of a new Raman peak with increasing concentration is LiCl, which has a characteristic peak at ~370 cm^{-1} (Table 1; Fig. 10). This peak has been previously observed in concentrated LiCl (and LiBr) solutions and have been interpreted to represent the Li–Cl stretching vibration of hydrated LiCl contact ion pairs (Rudolph et al., 1995). Hence, our results corroborate the formation of LiCl complexes with increasing concentration.

Amongst the alkaline earth chlorides, the only solutions to show emergence of any new Raman peaks with increasing concentration is $MgCl_2$, with a peak at ~356 cm^{-1}. This Raman peak in aqueous solutions containing magnesium has been previously interpreted to represent formation of explicitly hydrated $Mg(H_2O)_6^{2+}$ complexes (Irish, 1967; Ananthanarayanan, 1970; Pye and Rudolph, 1998). However, the peak position is similar to a weak Raman peak at 335-360 cm^{-1} observed in molten, anhydrous $MgCl_2$ (where formation of hydrated Mg complexes is obviously impossible), and has been interpreted to represent the symmetric stretching vibration of linear Cl–Mg–Cl complexes (Balasubrahmanyam, 1966; Huang and Brooker, 1976). Note also that Brewer et al. (1963) estimated a vibrational frequency of ~302 cm^{-1} for the same symmetric vibration of a linear $MgCl_2$ molecule in the gas phase. Although our result shows a mismatch of ~50 cm^{-1} compared to the latter result, we find similar offsets for several other metal dichlorides that probably reflect the difference in molecular environment between the condensed aqueous

liquid versus the gas phase, which are a known feature of comparisons between condensed versus gas-phase molecules (e.g., Spiekermann et al., 2012). Hence, we cannot rule out that the 356 cm^{-1} peak may represent hydrated magnesium species or Mg-Cl complexes, and the peak may indeed include contributions from both types of species.

In contrast to the alkalis and alkaline earths, *all* of the first-row transition metal chlorides (plus $SnCl_2$) show emergence of unique Raman peaks with increasing concentration. Manganese chloride solutions show emergence of a peak at ~355 cm^{-1}, which compares reasonably well with gas-phase theoretical calculations that estimated a symmetric stretching vibration of linear Cl–Mn–Cl molecules at 309 cm–1 (Brewer et al., 1963). A similar Raman peak position at 350 cm^{-1} was also observed in crystalline $MnCl_2 \cdot 2H_2O$ but was interpreted to represent the Mn–Cl "wagging" (bending) vibration of $MnCl_2$ (Srivastava et al., 1978). Regardless of whether this mode should be assigned to stretching or bending vibrations, it seems that there is general agreement that it represents vibrations between Mn and Cl, and we therefore interpret it to represent Mn–Cl complexes in concentrated solutions.

In the case of iron chlorides, we observe the emergence of unique Raman peaks in both $FeCl_2$ and $FeCl_3$ solutions, which are in both cases in good agreement with recent results at hydrothermal conditions by Scholten et al. (2019). Ferrous chloride solutions show a modest intensity Raman peak at ~368 cm^{-1}, which is in relatively good agreement with theoretical prediction for the symmetric stretching vibration of a linear, gas-phase Cl–Fe–Cl molecule at ~327 cm^{-1} (Brewer et al., 1963). Our result is also in good agreement with results by Bach et al. (1996), who estimated the symmetric stretch of a linear $FeCl_2$ complex to be at ~362 cm^{-1}. Notably, Scholten et al. (2019) observed that with increasing temperature, this Raman peak of $FeCl_2$ solutions dissipated and was replaced with a strong peak at ~280 cm^{-1}, interpreted to

represent hydrated, charged $FeCl_x^{2-x}$ complexes with explicit H_2O of solvation. In the case of $FeCl_3$ solutions, we observe the emergence of a very strong Raman peak at ~318 cm^{-1}, which matches well the observations by Scholten et al. (2019) both at ambient temperature and at hydrothermal conditions >300 °C. Scholten et al. (2019) interpreted this peak to represent explicitly hydrated, charged $FeCl_2^+$ complexes (based in part on previous work by Kanno and Hiraishi, 1982).

Cobalt chloride solutions show a characteristic Raman peak at 255 cm^{-1}. This peak probably represents the symmetric stretching vibration of Cl–Co–Cl complexes, which was previously estimated to occur at 267 cm^{-1} (Agullo-Rueda et al., 1987). Nickel chloride solutions show a characteristic Raman peak at 390 cm^{-1}. Again, this latter peak probably represents symmetric stretching of of Cl–Ni–Cl complexes, which was estimated to occur at 372 cm^{-1} (Agullo-Rueda et al., 1987; and at 326 cm^{-1} in the gas phase according to Brewer et al., 1963). Copper(II) chloride solutions show a modest Raman peak at ~287 cm^{-1}, which is almost certainly representative of copper chloride complexes in solution. This peak is absent in the case of crystalline $CuCl_2 \cdot 2H_2O$, but observed in anhydrous $CuCl_2$, and was interpreted in the latter case to represent Cl–Cu–Cl symmetric stretching (Medeiros et al., 2018). Other workers have interpreted the same peak as being representative of $CuCl_4^{2-}$ species (Suffren et al., 2011). In either case, the consensus is that the ~287 cm^{-1} peak represents chloride complexes of Cu^{2+}.

Zinc chloride solutions have been analyzed by Raman spectroscopy (as well as various X-ray techniques) in several previous studies—in part because $ZnCl_2$ shows anomalously high solubility in aqueous fluids compared to other metal halides—which provides a solid foundation for interpreting our observations. We find that a main new peak of $ZnCl_2$ solutions over a wide range of concentration >10 wt% occurs at ~294 cm^{-1}. This feature was previously reported by

Irish et al. (1963) who interpreted it as having two components: a peak centered at ~278 cm^{-1} and assigned to hydrated $ZnCl_4^{2-}$ complexes, plus another peak centered at ~305 cm^{-1} and assigned to ZnCl+ and $ZnCl_2$(aq). A Raman peak at this position was also observed in anhydrous $ZnCl_2$ melts (Alsayoud et al., 2016), where hydrated $ZnCl_4^{2-}$ obviously cannot be formed and in this context, must be assigned to $ZnCl^+$ and $ZnCl_2^0$. At very high concentrations of $ZnCl_2$ (>70 wt%), we see the emergence of two additional Raman peaks, one centered at ~242 cm^{-1}, and the other at ~3500 cm^{-1} and overlapping with the O-H stretching region of H_2O. The peak at ~242 cm^{-1} was also previously noted by Irish et al. (1963), who related this Raman peak to the formation of polynuclear aggregates, or clusters of ions sharing a local environment similar to the structure of crystalline $ZnCl_2$. This latter peak is also the most prominent Raman feature of molten, anhydrous $ZnCl_2$ (Alsayoud et al., 2016), which is also consistent with the interpretation that this peak represents large clusters, perhaps heralding the approach to salt saturation and nucleation of crystals as seen in Na_2SO_4 solutions (Reimer et al., 2015). Finally, the Raman peak at 3500 cm^{-1} that emerges at >70 wt% $ZnCl_2$ likely represents formation of $Zn(H_2O)_6^{2+}$ species at high concentrations (Irish et al., 1963).

The $SnCl_2$ solutions show a distinct, narrow peak at 270 cm^{-1} which increases with intensity relative to the O-H stretching region as concentration increases. A similar peak was noted by Schmidt (2018) at 275 cm^{-1}. This peak was described as being the Sn(II)-Cl vibration in aqueous solution, which was lower in intensity than the Sn(IV)-Cl vibrations observed by Schmidt (2018). Additionally, an increase in Raman intensity was observed at 220 cm^{-1} with increasing concentration, which Schmidt (2018) interpreted as the formation of $SnCl_3^-$ ion pairs. Finally, the concentrated $SnCl_2$ solutions show a Raman peak at ~2800 cm^{-1}, the same as seen in

the HCl solutions, which reflects the fact that the studied $SnCl_2$ solutions were prepared with equimolar HCl:$SnCl_2$ in order to solubilize the tin(II).

Finally, in the case of NH_4Cl, we observe the internal bending modes (1435 and 1700 cm^{-1}) and stretching modes (2885 cm^{-1} and 3070 cm^{-1}) of the ammonium ion (which are also evident in crystalline salammoniac), but we emphasize that these peaks are not diagnostic of ion pairing as they are characteristic of the polyatomic NH_4^+ ion itself (Krishnan, 1947).

4.2.2 Insights into geochemical factors that influence ion pair formation

Numerous studies have contemplated the root causes, at the molecular scale, for why certain cation-anion combinations spontaneously form ion pairs whereas others do not (Collins, 1997; Marcus, 2005; Collins, 2006; Marcus and Hefter, 2006; Lund et al., 2009). In this context, it is important to note that ion association in aqueous solution is generally thought to be a stepwise process, wherein initially free, fully solvated ions first approach one another to form solvent-separated (and thus, non-bonded) ion pairs (SSIP), and only if the intervening H_2O molecules are expelled do (bonded) contact ion pairs form (CIP; Eigen and Tamm, 1962). This distinction between loosely associated SSIP versus explicitly bonded CIP is critical to interpretation of the Raman spectroscopic results, because only CIP will show characteristic Raman peaks, owing to the requirement of some degree of explicit donor-acceptor electron sharing for the Raman effect (Marcus and Hefter, 2006). Stated differently, the chloride salts that show characteristic Raman peaks in Table 1 (except for NH_4Cl) are those that form CIP in aqueous solution at 25 °C and 1 bar. Therefore, our results can provide some insight into the underlying factors that differentiate cations that form CIP with Cl^- versus those that do not.

Collins (1997) observed that ionic radius is a critical factor affecting whether or not certain cation-anion combinations will spontaneously form ion pairs. In the case of ions of equal charge, the average surface charge density obviously increases with decreasing ionic radius, and hence ions of smaller radius have strong attraction to H_2O of solvation, but even stronger attraction to ions of opposing charge. Collins (1997; 2006) thus established empirically certain threshold radii that separate cations and anions that are likely to form pairs versus those that are not. In the case of cations, Collins (1997; 2006) placed the threshold radius at approximately the value of the effective radius of an H_2O molecule, 106 pm—thus, cations of a radius <106 pm are expected to exhibit strong affinity to form ion pairs with small anions (Collins, 2006; Lund et al., 2009). In the case of anions, the threshold radius separating "big" and "small" anions is approximately 178 pm (Collins, 1997; 2006). Amongst the solutes studied here, the anion is invariably Cl^-, whose ionic radius in aqueous solution is estimated to be ~181 pm (Marcus, 1991), and thus sitting almost exactly on the margin between "big" and "small" (Collins, 1997). Consequently, the principal factor that would be expected to differentiate solutes showing explicit CIPs versus those that do not, at least in the case of the 1:1 electrolytes, is radius of the cation. Indeed, we find this to be the case, such that amongst the monovalent cations (alkalis and ammonium), only H^+ and Li^+ have radii <100 pm and these are the only chlorides to show evidence of CIP formation (Fig. 11).

In the case of divalent and trivalent cation chlorides (1:2 and 1:3 electrolytes), direct application of the conceptual model of Collins (1997; 2006) is somewhat ambiguous because the average surface charge density on the cation does not only scale with ionic radius, but also with charge. Stated differently, the cations of higher charge obviously have higher charge density than their monovalent counterparts of comparable size, and hence we might intuitively expect that the

critical factor that distinguishes pair formers would be the ratio of charge/radius (rather than ionic radius alone). However, our results do not seem to support this suggestion, and instead we find that the same threshold radius of ~100 pm for the cation seems to hold regardless of charge on the cation (Fig. 11). Hence, our results suggest empirically that in the case of chloride salts, those with cations larger than or equal in size to sodium and calcium generally do not form ion pairs, whereas those with smaller cations do. A phenomenological explanation for this empirical (and somewhat unintuitive) observation is of interest for predictive modeling, and so we provide some speculative discussion here.

To rationalize our observation that ionic radius alone is the decisive factor regarding ion pair formation, rather than the charge/radius ratio, we consider the implied geometry of coordination by solvent H_2O of the hydrated cations according to Pauling's Rules (Fig. 11B; Pauling, 1929). We emphasize that Pauling's Rules strictly apply to coordination of ions in crystalline materials, and we apply these rules here only as a simplified conceptual model to help visualize how solvation and ion association may differ in the case of "big" versus "small" cations. Essentially, according to Pauling's Rules, a smaller cation can only be closely surrounded by fewer anions of equal size, potentially leaving relatively large gaps or holes in the first coordination shell. In contrast, larger cations can be closely surrounded by a greater number of anions of equal size, which can be envisioned as giving rise to an unbroken first coordination shell (without holes). Hence, from this conceptual point of view, a sparse first coordination shell around a cation of smaller ionic radius enables a chloride anion to access the cation (Fig. 11B), thus forming a CIP. In contrast, the cation of larger ionic radius is surrounded by more H_2O's of solvation such that no interstitial gaps remain. In this case, the solvation shell effectively shields the cation and does not allow chloride ions to access the cation, preventing formation of CIPs.

Again, we emphasize that this conceptual model is highly simplified and is not meant to quantitatively describe real molecular-scale interactions, but we nevertheless suggest that this view at least provides a plausible mechanistic explanation as to why ionic radius seems to be more important than charge/radius ratio in determining ion pair formation.

4.3 Salinity Estimation

4.3.1 Bulk Salinity Estimates

Since the 1960's, numerous workers have developed various calibration schemes relating the relative Raman intensities of various peaks to the absolute salinity (Busing and Hornig, 1961; Schultz and Hornig, 1961; Walrafen, 1962; Mernagh and Wilde, 1989; Baumgartner and Bakker, 2009; Sun et al., 2010; Frezzotti et al., 2012). Most such calibrations for salinity estimates of aqueous fluids have been based on the relative integrated intensity (or peak areas), quantified by peak fitting functions (Walrafen, 1962; Mernagh and Wilde, 1989; Sun et al, 2010), with focus mostly on the relative intensities particularly between "network" (hydrogen-bonded) versus "poorly connected" (weakly hydrogen bonded, with few neighbors) H_2O—or in other words, the relative intensities of the shoulder at ~3250 cm^{-1} versus the main peak of H2O at ~3380 cm^{-1}. However, as noted above a variety of interpretations and models for the O-H stretching region of H_2O have been proposed, and there is little consensus on the true number of peaks, their relative intensities, nor their positions. Inevitably, this uncertainty introduces a number of questions with regard to how to treat the O-H stretching region in terms of estimating salinity.

Arguably the most comprehensive development of a Raman spectroscopic salinity sensor to date was that of Sun et al. (2010), who evaluated the effect of salinity on the shape of the O-H

stretching region for four geologically relevant chloride salts: NaCl, KCl, $CaCl_2$, and $MgCl_2$. Remarkably, Sun et al. (2010) found that when the salinities of these four salts were expressed in terms of molar concentration of chloride (moles of Cl per litre of solution), all four salts conformed to a single calibration equation—thus, potentially allowing for salinity estimates independently of the identities of the cations in chloride-rich brines. Although not explicitly discussed by Sun et al. (2010), the use of molarity units of concentration in this context makes intuitive sense, because molarity units implicitly account for the degree of electrostriction, and hence the solute-solvent interactions that are also manifested in the distortion of the O-H stretching region. In the latter regard, the approach by Sun et al. (2010) is analogous to the approach by Lamadrid et al. (2018) and Sublett et al. (2020) to estimate fugacities of species in gas mixtures. Here, because we analyzed the same salts as done by Sun et al. (2010) but with more coverage in terms of salinity, as well as a wide variety of other chloride salts, we tested the application of the equation provided by Sun et al. (2010) to our data. To do so, we applied the same two-peak fitting procedure as described by Sun et al. (2010), and transformed our salinities into units of molarity of chlorine using the solution density data shown in Table 2.

Results of our comparison showed an excellent linear relationship between the known (measured by gravimetry) salinity versus that predicted by Raman spectroscopy using the equation of Sun et al. (2010), but this linear relationship did *not* conform to a 1:1 line (Fig. 12). Stated differently, we found that the equation from Sun et al. (2010) systematically underestimated the molar concentration of Cl by ~22% across the whole range of concentration for NaCl, exhibiting an excellent linear fit with high R^2 (>0.99). We attribute this systematic mismatch to the same factors as discussed by Lamadrid *et al*. (2017), De Vitre et al. (2021) and Remigi *et al*. (2021), who all noted that density calibrations for CO_2 based on Raman spectra

commonly differ to a significant degree between different Raman instruments. The exact reasons for these inter-laboratory differences in Raman calibrations are only partly understood, but probably reflect subtle differences in parameters that might include laser wavelength, room temperature/humidity, and precise position of each relevant pixel of the instrument CCD detector. These and other factors likely introduce subtle differences in each individual spectrometer, which can have significant effects on quantitative calibrations. As our results of comparison with the equation of Sun et al. (2010) show an excellent linear correlation but a systematic underestimation of salinity, we conclude that the salinity calibration shows similar variations as seen for gas densimeters. Therefore, we strongly suggest that, in order to use Raman spectroscopy for salinity estimation, each laboratory should consider analyzing solutions of known salinity to develop their own, laboratory-specific calibration (Lamadrid et al., 2017 and De Vitre et al., 2021). In the next paragraphs, we outline the approach to calibration taken here, which may be promising for such developments.

Our initial attempts at calibrating a Raman spectroscopic salinity sensor for aqueous fluids used the same two- peak model for the O-H stretching region as done by Sun *et al*. (2010). However, we noted that the residuals of the model fits were rather poor (see, for example, Fig. 3 of Sun et al., 2010). These poor residuals introduced significant error for many of the solutes studied here that showed different shapes of the O-H stretching region. However, our attempts using a five-peak model (e.g., Sun, 2009) were similarly unsatisfying because the broad and overlapping peaks could not be confidently disentangled in a way that worked consistently across the different solutes and from dilute to concentrated solutions. Therefore, we experimented with a different approach that avoids peak fitting altogether, by calibrating a numerical relationship between salinity and relative intensities at specific Raman shifts. This

approach was previously used successfully to calibrate the NaOH concentrations of aqueous solutions because the Raman peak for hydroxide overlaps with the O-H stretching region of H_2O (Shaffer, 1997; Steele-MacInnis and Schmidt, 2015). Here, we adapt this approach to estimate molal concentration of chloride across a wide range of chloride-salt solutes.

In our straightforward procedure, we first performed a linear baseline subtraction and then simply extracted the intensity at four positions (Raman shifts) across the O-H stretching region: 2800, 3250, 3380 and 3640 cm^{-1}. The outer two positions (2800 and 3640 cm^{-1}) were selected primarily as "anchors," to compute relative heights of the two inner positions at 3250 and 3380 cm^{-1}, which roughly correspond to strongly hydrogen bonded and weakly hydrogen bonded H_2O, respectively. Hence, the ratio of these two peak heights is a measure of the relative degree of hydrogen bonding, and thus a proxy measure of salinity. Finally, for each datum amongst the saline fluids, we subtracted the same ratio of pure H_2O to effectively zero the y-intercept. The resulting calibration equation thus has the form:

$$m_{Cl} = A\left(\left(\frac{i_{3380}-i_{3640}}{i_{3250}-i_{2800}}\right)_{Sample} - \left(\frac{i_{3380}-i_{3640}}{i_{3250}-i_{2800}}\right)_{H2O}\right) \quad (1)$$

where m_{Cl} denotes molality of chloride; i_x denotes Raman intensity at the wavenumber denoted by the the subscript x; and A is a single empirical coefficient (specific to each Raman spectrometer) determined by linear regression analysis.

First, we applied this simple calibration equation to our data on the same four salts as studied by Sun et al. (2010), in order to test whether a molarity scale (as used by Sun et al., 2010)

provides a better quantitative fit than the more convenient molality scale (Fig. 13 A, B). Our results showed, somewhat unexpectedly, that the calibration works equally well regardless of whether molal or molar units are used (Fig. 13 A, B), and in fact the data show a slightly better linear relationship when molal units are used instead of molar. Because molarity units are per litre of *solution*, and because molar volumes of aqueous solutions vary strongly with temperature and pressure, molar units are generally inconvenient in geologic applications. Therefore, based on our results, we suggest that salinity calibrations based on Raman spectra should generally use *molal* units, as the latter are independent of fluid density and indeed yield a slightly improved fit. We also note that because our data included a wider range of concentrations compared to Sun et al. (2010), the trends for $CaCl_2$ and $MgCl_2$ diverge at high salinities >6 molal Cl (Fig. 13A, B). Sun et al. (2010) had analyzed $CaCl_2$ solutions up to ~9 molal Cl, but $MgCl_2$ solutions only up to ~3 molal Cl, and therefore did not observe this divergence. It should be emphasized that Mg-rich bittern brines with $MgCl_2$ concentrations up to 3 molal Mg (hence, ~6 molal Cl) have been reported in unconformity-type U deposits (Richard et al., 2010; Mercadier et al., 2012).

Next, we used the same approach to test the calibration of Eq. 1 amongst the other chloride salts (Fig. 13C). As noted above, Sun et al. (2010) observed and discussed how the Raman spectral salinity sensor, when expressed in terms of molar concentration of chloride, seemed to apply equally as well regardless of the identities of the cations, though this was based only on the chlorides of Na, K, Mg and Ca. Therefore, we tested how well this same approach would apply across a wider spectrum of chloride salts. Our results show that, when all 19 salts are plotted over the full range of concentrations analyzed, a single linear relationship does not hold, and instead the data display a "fan" shape wherein the trends for individual salts diverge strongly towards high salinity (Fig. 13C)—similar to, but more pronounced, the divergence

between the results for $CaCl_2$ and $MgCl_2$ noted above. This result can be rationalized by considering the relationship between the Raman spectrum of solvent H_2O and salinity essentially similar to the well-known *colligative properties* of electrolyte solutions (e.g. freezing point depression, boiling point elevation, osmotic coefficient), each of which conform to universal relationships with molal concentration (independent of the identity of the electrolyte solute) at low salinity, but diverge strongly at high concentration. Moreover, of the 19 chloride salts studied here, 7 display particularly strong departure from the common linear trend: CsCl, $MnCl_2$, $FeCl_3$, $CoCl_2$, $CuCl_2$, $ZnCl_2$, and $SnCl_2$. Each of these latter salts, at high concentration, show trends that tend to plateau, such that the peak intensity ratio no longer varies with salinity when concentration is high (Fig. 13C). As a result, a direct application of Eq. 1 to these solutions at high concentration would yield significant underestimates of chloride concentration. We interpret the root causes for the strong divergence of these latter 7 salts as follows. In the case of CsCl, the divergence is likely a result of the large ionic radius and low charge of the cation, such that Cs^+ shows a weaker attraction to solvent H_2O and therefore less tendency to electrostriction of H_2O. In contrast, in the case of $MnCl_2$, $FeCl_3$, $CoCl_2$, $CuCl_2$, $ZnCl_2$, and $SnCl_2$, these chlorides show strong tendency to form ion pairs (as evidenced from their respective Raman peaks at low wavenumber), and as a result these solutes effectively yield fewer free ions per mole of salt than would be predicted based on stoichiometry alone. We note also that CsCl, $MnCl_2$, and $ZnCl_2$ diverge from the common trend above ~6 molal, whereas the threshold concentrations for $FeCl_3$, $CoCl_2$, $CuCl_2$, and $SnCl_2$ are lower, ~2-4 molal.

Our results reaffirm, as suggested by Sun et al. (2010), that a single calibration of the relationship between chloride concentration and shape of the O-H stretching band of H2O can be an effective tool to estimate salinity of brines independently of the type(s) of chloride salts in

solution over wide ranges of concentration. For 12 of the 19 salts, we find that a single calibration works over the whole salinity range from dilute to saturated solutions—which, in many cases (e.g., RbCl, NH_4Cl, $BaCl_2$ etc.), is a significantly wider range than the whole range of known geologic fluid compositions. Stated differently, a straightforward calibration such as Eq. (1) will hold for these 12 salts at *any* concentration expected in geologic fluids. Even in the case of ferrous iron ($FeCl_2$), which has been reported in magmatic-hydrothermal fluids such as in porphyry Cu deposits at concentrations up to 10's of wt% (Yardley, 2005; Bodnar et al., 2014; Audétat, 2019), the same straightforward, linear calibration holds across this full range of Fe concentrations. Fortunately, even in the case of the 7 salts that show significant departure from the simple calibration at high salinity, such departures are unlikely to affect analyses of natural fluids because of the limited ranges of concentrations of these salts reported in geologic fluids. For example, Cs concentrations are generally highest in fluids exsolved from highly evolved granitic pegmatites, but to our knowledge the highest concentrations reported from brine inclusions in such settings were ~2 wt% (~0.1 molal Cl; Borisova et al., 2012). Manganese concentrations in brine inclusions from magmatic-hydrothermal ore deposits commonly reach multiple wt% levels (up to ~7 wt% Mn, corresponding to ~1 molal Cl; Yardley, 2005; Audétat, 2019), which again is well within the range of concentration over which our calibration holds for $MnCl_2$. With regard to $FeCl_3$, the highest Fe concentrations (10's of wt%) reported tend to be from porphyry Cu deposits that are generally oxidized and where primarily ferrous iron is expected, but nevertheless even at concentrations up to ~20 wt% $FeCl_3$ our calibration still holds. Concerning Co, to our knowledge the highest Co concentration reported from natural fluid inclusions was ~1000 ppm (0.1 wt%, or ~0.02 molal Cl; Davey et al., 2021), well within the working range of our calibration. Brine inclusions from various magmatic-hydrothermal ore

deposits have shown reported concentrations of up to ~3 wt% Cu (Steele-MacInnis et al., 2021), ~1 wt% Zn (Audétat, 2019) and ~1 wt% Sn (Van Daele, 2018), but even such extreme metal chloride concentrations are well within the range of validity in our calibration equation for $CuCl_2$, $ZnCl_2$ and $SnCl_2$. Hence, we conclude that some solutes should be analyzed cautiously using the approach outlined here, but at least in terms of geologic fluids reported so far it appears that a common salinity calibration will apply in most circumstances.

Overall, our results support the general approach outlined by Sun et al. (2010) and suggest a somewhat more straightforward procedure that uses only peak intensities rather than peak areas, as well as molal concentration rather than molar. Our results also show that a relatively simple (linear) relationship between ratios of peak intensities and chloride concentration holds independently of the identity of the cation, at least up to modest concentrations of most common geologic solutes. This approach to quantifying bulk salinity might hold particular promise when combined with additional information on the ratios of cations in a fluid inclusion, for example by laser ablation ICPMS (Steele-MacInnis et al., 2016). That said, we stress that the application of such a Raman spectroscopic salinity proxy to fluid inclusions in minerals must also account for other potential sources of uncertainty, and in particular the effect of the mineral host on the Raman spectrum. Previous studies have shown that the optical polarization of the host mineral can have a significant impact on the measured peak ratios of the O-H stretching region of H_2O (Baumgartner and Bakker, 2009; Sun, *et al*, 2010), and such variations would implicitly propagate into salinities estimated by the approach discussed here. Finally, we reiterate that the fitting coefficient in Eq. (1) is almost certainly instrument specific (Lamadrid et al., 2017; De Vitre et al., 2021; Remigi et al., 2021), and therefore each laboratory must develop their own calibration. In this regard, the general

consistency of the trends amongst different chloride salts is a definite advantage, because a calibration based only on a single solute (e.g., NaCl) will generally work well regardless of the types of chloride solutions analyzed in most cases.

4.3.2 Individual Salt Molality Estimates

As noted in the previous section, the formation of ion pairs amongst solutes such as $CuCl_2$, $ZnCl_2$ and $SnCl_2$ poses some challenge for bulk salinity estimation owing to a subdued effect of these latter solutes on the O-H stretching band of H_2O at high salinity (Fig. 13C). However, at the same time this phenomenon creates an opportunity to develop tools to quantitatively estimate the concentrations of these solutes based on the relative intensity of each relevant, unique Raman peak assigned to the latter ion pairs. To do so, we tested how the ratio of the peak intensity for each relevant peak, compared to the intensity of the O-H stretching band, varied with concentration, similar to Eq. (1). The general equation for such a calibration can be expressed as:

$$m_{XCl2} = B_X\left(\left(\frac{i_{\text{ion pair}}}{i_{3380}}\right)_{\text{Sample}} - \left(\frac{i_{\text{ion pair}}}{i_{3380}}\right)_{H2O}\right) \quad (2)$$

where X represents either Cu, Zn or Sn (or, potentially, other cations whose chlorides show Raman spectroscopic evidence of ion pairing), B_X is a regression coefficient specific to each latter solute, and $i_{\text{ion pair}}$ represents the Raman intensity at 287, 294 or 270 cm^{-1} (respectively; Fig. 14A–C). In the case of $CuCl_2$, the peak intensity ratio for the 287 cm–1 peak

remains essentially zero until a threshold concentration of 1 molal Cl is exceeded, suggesting that this is the threshold concentration for the onset of ion pairing of $CuCl_2$ (Fig. 14A). In contrast, the respective peak intensity ratios for both $ZnCl_2$ and $SnCl_2$ increase monotonically at all measured concentrations above pure H_2O (Fig. 14B, C). These results suggest that the relative intensities of the peaks specific to ion pairs may be a promising avenue not just for identifying, but also quantifying concentrations, of some salts that show ion pairing. Such an approach may be particularly useful for situations where LA-ICP-MS techniques cannot be used due to interferences from the host mineral, such as in the case of analysis of zinc in fluid inclusions hosted in sphalerite (Szmihelsky et al., 2021).

Another potentially impactful, potential calibration with regard to individual solutes in solution is the possibility of estimating HCl concentrations—and hence, pH—of geologic fluids. Dubessy et al. (1992) developed an approach to estimating pH of fluid inclusions indirectly, according to the relative peak areas corresponding to carbonate and bicarbonate and the known pH-dependent homogeneous equilibrium between these species in solution. However, our results suggest a potential direct alternative according to the Raman intensity at ~2800 cm^{-1} corresponding to HCl ion pairs. Similarly to Eqs. (1) and (2), we can express a simple calibration equation based on the relative peak intensity of the latter peak as follows:

$$m_{\mathrm{HCl}} = C\left(\left(\frac{i_{2800}}{i_{3250}+i_{3380}+i_{3640}}\right)_{\mathrm{Sample}} - \left(\frac{i_{2800}}{i_{3250}+i_{3380}+i_{3640}}\right)_{\mathrm{H2O}}\right) \quad (3)$$

where m_{HCl} is the molal concentration of HCl and C is a fitting coefficient. In Eq. (3), note that the intensity of the 2800 cm–1 peak of HCl is compared to the *sum* of three peak positions

corresponding to the O-H stretching band of H_2O, in order to exclude generally effects of bulk salinity on the shape of the O-H stretching band. Indeed, we find that the HCl data conforms well to a simple linear correlation according to Eq. (3), whereas the neutral salts NaCl, KCl, $MgCl_2$ and $CaCl_2$ show essentially zero values across the whole range of salinity (Fig. 14D). To test the application of this approach beyond the calibration, we used Eq. (3) to calculate the (known) concentration of HCl in the $SnCl_2$ solutions (Fig. 14E). The results show a good positive correlation with a slope close to 1:1, indicating that Eq. (3) provides reasonable estimation of the HCl concentration. We suggest that this approach can be coupled with the known relationship between HCl concentration and pH to serve as a direct, spectroscopic pH sensor for geologic brines.

5. Conclusions

We surveyed the Raman spectroscopic properties of aqueous metal-chloride solutions at ambient temperature and pressure for 19 chloride salts, from pure H_2O up to salt saturation. The results show that Raman spectra can be used to reasonably estimate salinity across wide ranges of salt types and salinities, likely encompassing the whole range encountered in natural geologic fluids. Some salts specifically affect the O-H stretching region, whereas others show explicit spectroscopic evidence for ion pair formation. We found that the likelihood that a cation will form an ion pairs with chloride in solution is strongly dependent on the ionic radius (with the threshold at ~100 pm), and apparently independent of the charge of the cation. The specific Raman peaks indicative of the various ion pairs (Table 1) can in some cases be used to identify certain solutes in solution.

In terms of salinity estimation, we built upon the previous study of Sun *et al*. (2010) and show that a similar (and in fact, even more straightforward) relationship between peak intensity ratios and molal concentration of chloride is valid for most chloride salts over wide ranges of concentration. Some salts, such as $FeCl_3$, $CuCl_2$, $SnCl_2$, and $CoCl_2$ diverge from the common trend when salinity is high, likely due to formation of ion pairs that effectively reduce the molal concentration of free Cl^-, but generally this occurs only at concentrations that exceed what has been reported for geologic fluids. Meanwhile, the formation of such ion pairs potentially enables individual calibrations that could be used to quantify certain metal contents, and even pH, by spectroscopic means (Fig. 14). We emphasize that such calibrations for salinity, pH and metal contents should probably be performed for each specific laboratory and instrument owing to the previously noted differences between quantitative Raman sensors for other parameters like gas densities, and we suggest that the approaches outlined here and Eqs. (1) through (3) can serve as a guide for such developments.

TABLES

Table 1. Conditions of the experiments, and the peak positions of the main observed Raman peaks that are distinct from the spectrum of pure H_2O.

Compound	Concentration Range (wt%)	Measurement interval (wt%)	Diagnostic peaks (cm^{-1})
HCl	0 - 37	5	2800
LiCl	0 - 45	2	370
NaCl	0 - 26	1	-
KCl	0 – 25	1	-
RbCl	0 – 47	10	-
CsCl	0 - 65	5	-
$MgCl_2$	0 - 34	2	356
$CaCl_2$	0 - 43	2	-
$SrCl_2$	0 - 34	10	-
$BaCl_2$	0 - 25	5	-
$MnCl_2$	0 - 39	2	355
$FeCl_2$	0 - 40	5	368
$FeCl_3$	0 - 47	10	318
$CoCl_2$	0 - 33	2	255
$NiCl_2$	0 - 30	2	390
$CuCl_2$	0 - 43	2	287
$ZnCl_2$	0 - 80	10	294
$SnCl_2$	0 - 45	2	220, 270
NH_4Cl	0 - 28	2	1435, 1700, 2885, 3070

Table 2. Table of densities and their corresponding fitted equations. X is mole fraction and Y is density in g/cm^3.

Compound	Density Range (g/cm^3)	Density Equation
HCl	1 – 1.1736	$y = -1.0013x^2 + 0.87x + 1.0016$
LiCl	1 – 1.2947	$y = -0.3899x^2 + 1.2254x + 1.0012$
NaCl	1 – 1.1964	$y = -7.0855x^2 + 4.9167x + 1.0274$
KCl	1 – 1669	$y = 0.0068x + 0.9969$
RbCl	1 – 1.3853	$y = 0.6501x^2 + 4.2269x + 1.0025$
CsCl	1 – 1.4147	$y = -11.342x^2 + 7.0217x + 1$
$MgCl_2$	1 – 1.3287	$y = 3.6096x + 1.0084$
$CaCl_2$	1 – 1.4478	$y = -4.5272x^2 + 4.514x + 1.0053$
$SrCl_2$	1 – 1.1815	$y = -59.386x^2 + 8.2067x + 1$
$BaCl_2$	1 – 1.2748	$y = 9.4774x + 1.0024$
$MnCl_2$	1 – 1.4069	$y = 0.0104x + 0.9995$
$FeCl_2$	1 – 1.4483	$y = -7.4165x^2 + 3.7675x + 1.0013$
$FeCl_3$	1 – 1.5296	$y = -5.5463x^2 + 3.5456x + 1.0023$
$CoCl_2$	1 – 1.3600	$y = 5.6515x + 1.0069$
$NiCl_2$	1 – 1.3447	$y = -10.484x^2 + 6.7715x + 0.9993$
$CuCl_2$	1 – 1.5018	$y = -6.7928x^2 + 6.3701x + 1.0023$
$ZnCl_2$	1 – 1.9035	$y = -7.0855x^2 + 4.9167x + 1.0274$
$SnCl_2$	1 – 1.5944	$y = -16.609x^2 + 8.7498x + 1.0024$
NH_4Cl	1 – 1.0800	$y = -1.4781x^2 + 0.8549x + 1.0006$

FIGURES

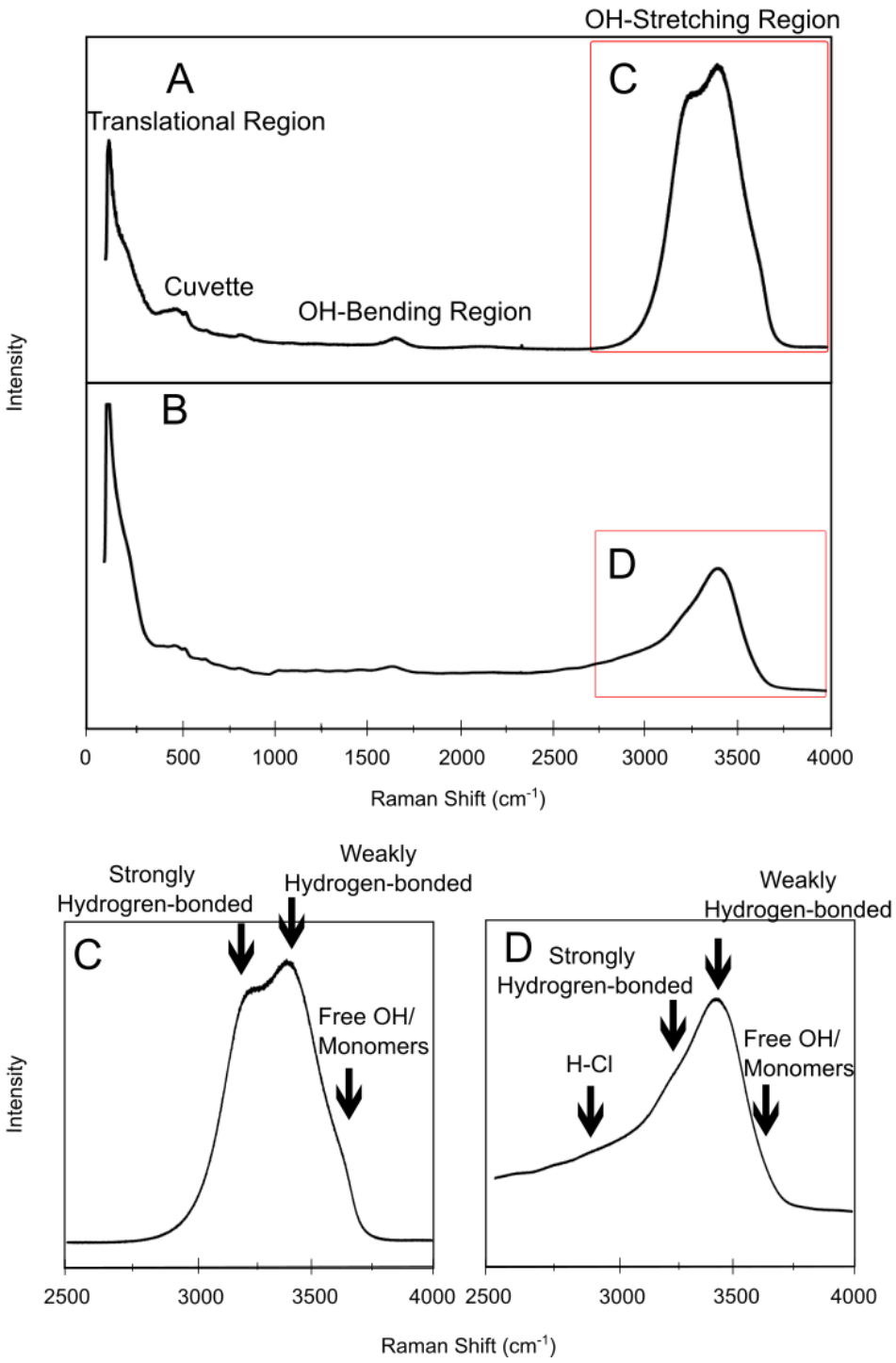

Figure 1. Regions of the Raman spectrum of water and their interpretations (see Section 1 for additional details).

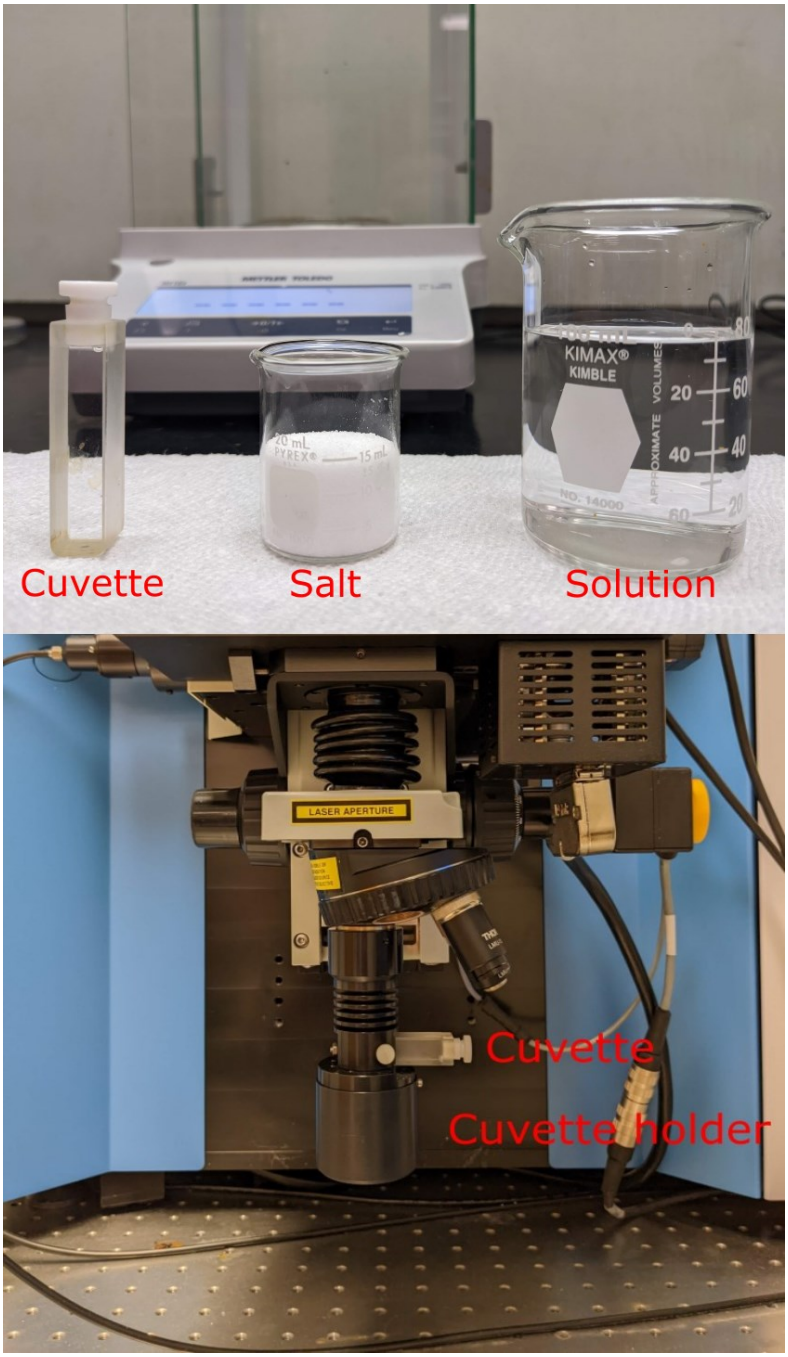

Figure 2. Photographs showing the configuration used in the experiments. In the lower photograph, the cuvette holder is attached to the lens revolver.

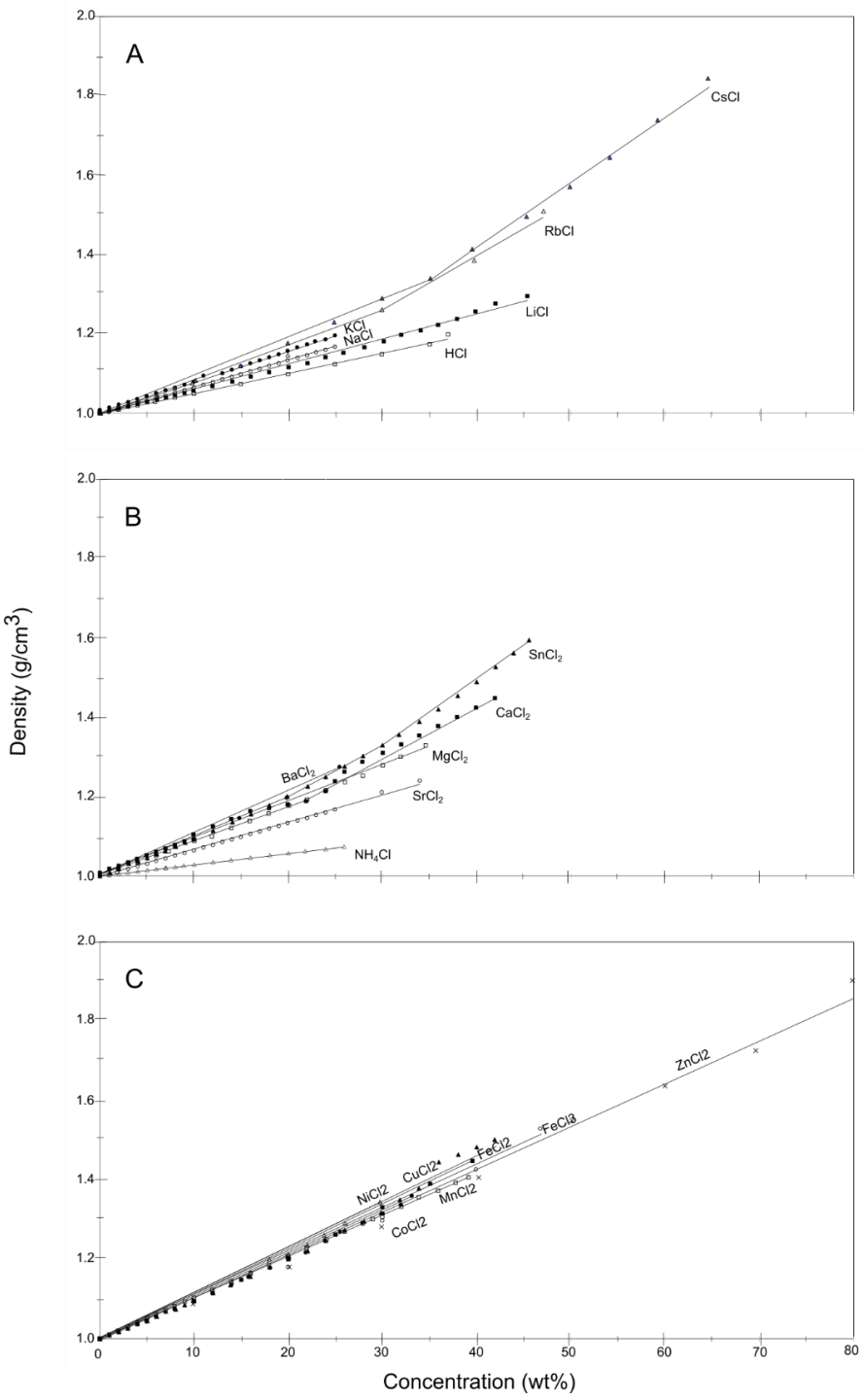

Figure 3. Concentrations of chloride salt solutions versus the density of each solution. A) Alkalis, B) Alkaline Earth metals (plus ammonium and tin(II)), C) First row transition metals.

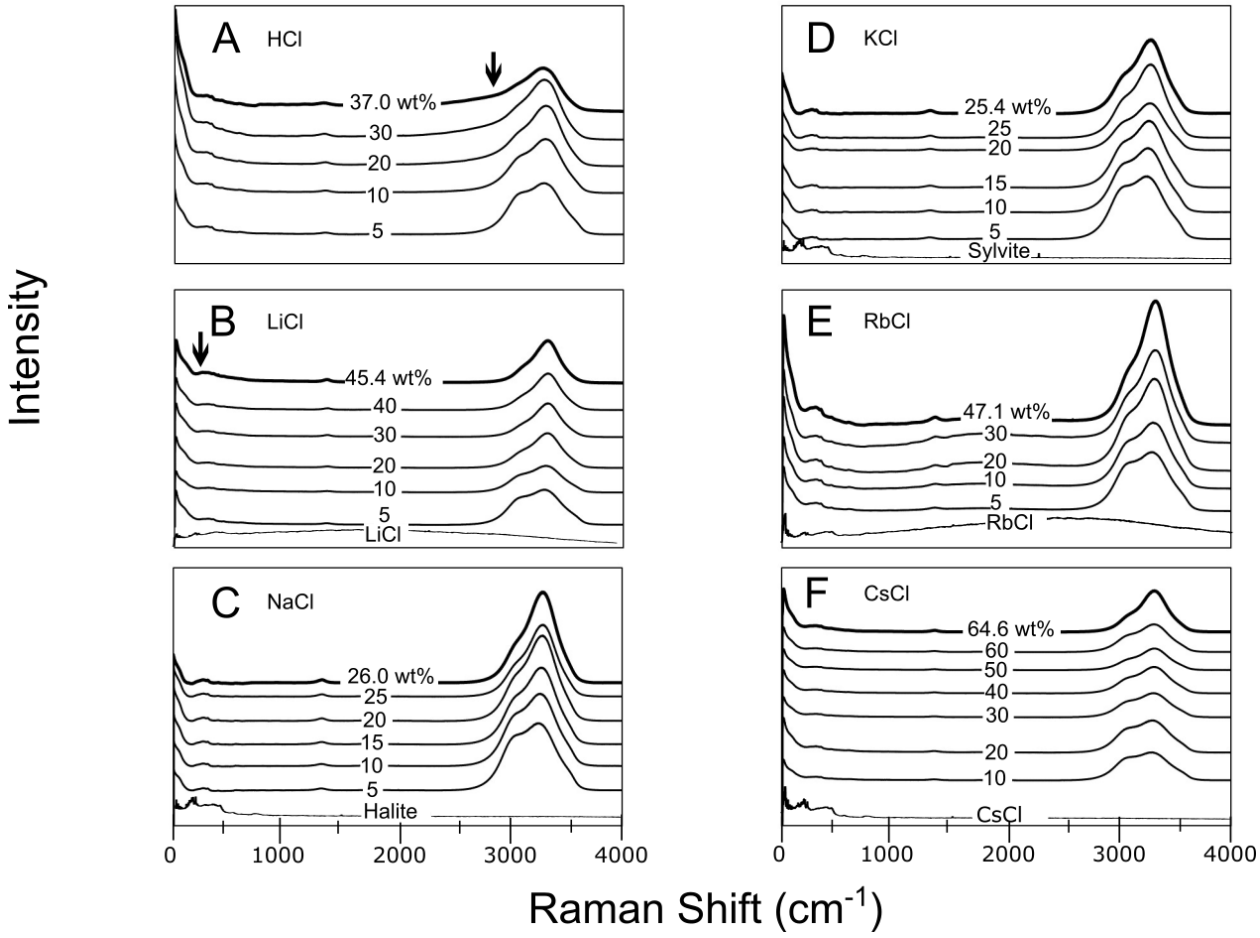

Figure 4. Raman spectra of alkali chlorides from 50 to 4000 cm^{-1}. A) HCl, B) LiCl, C) NaCl, D) KCl, E) RbCl, F) CsCl.

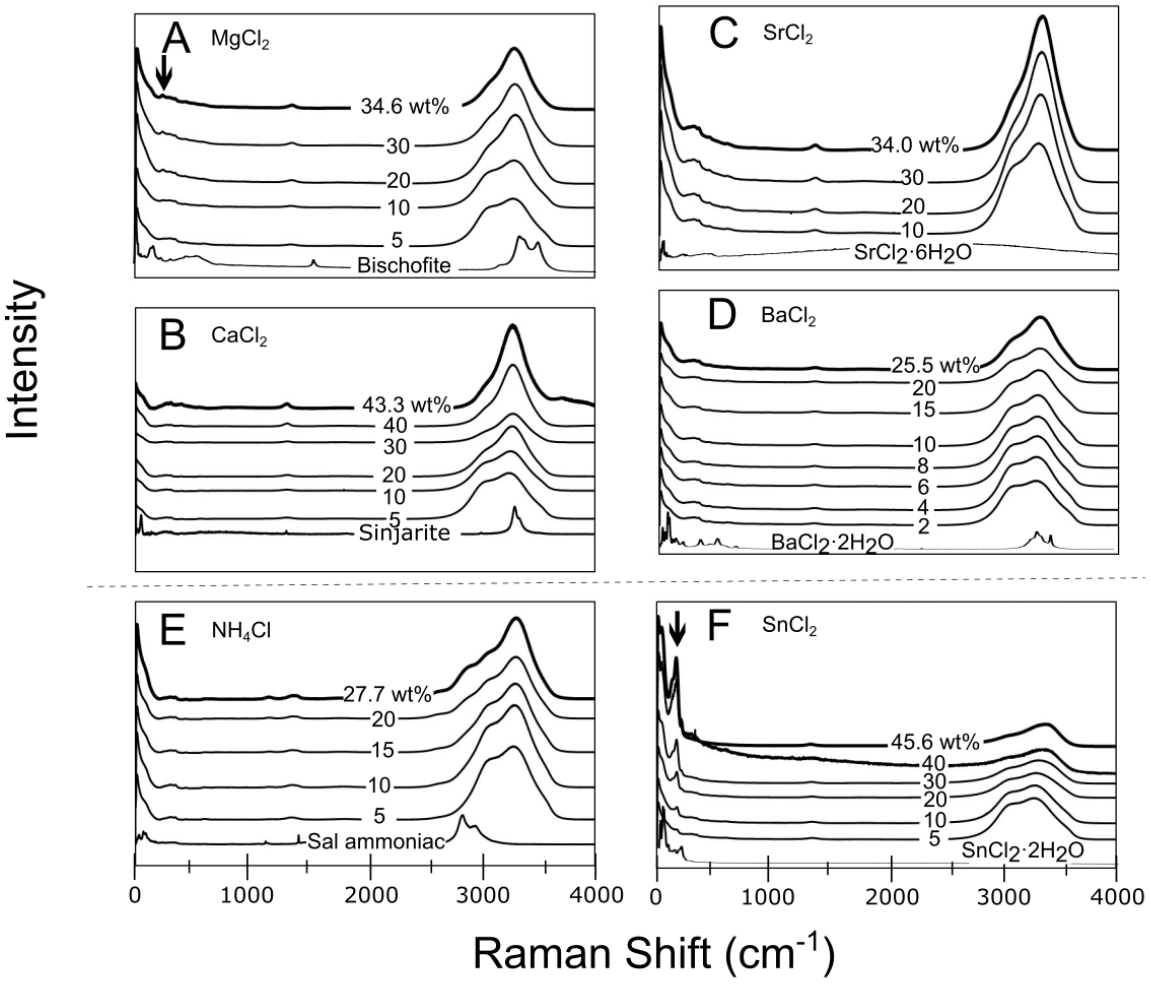

Figure 5. Raman spectra of alkaline Earth metal, ammonium and tin(II) chlorides from 50 to 4000 cm^{-1}. A) $MgCl_2$, B) $CaCl_2$, C) $SrCl_2$, D) $BaCl_2$, E) $SnCl_2$, F) NH_4Cl.

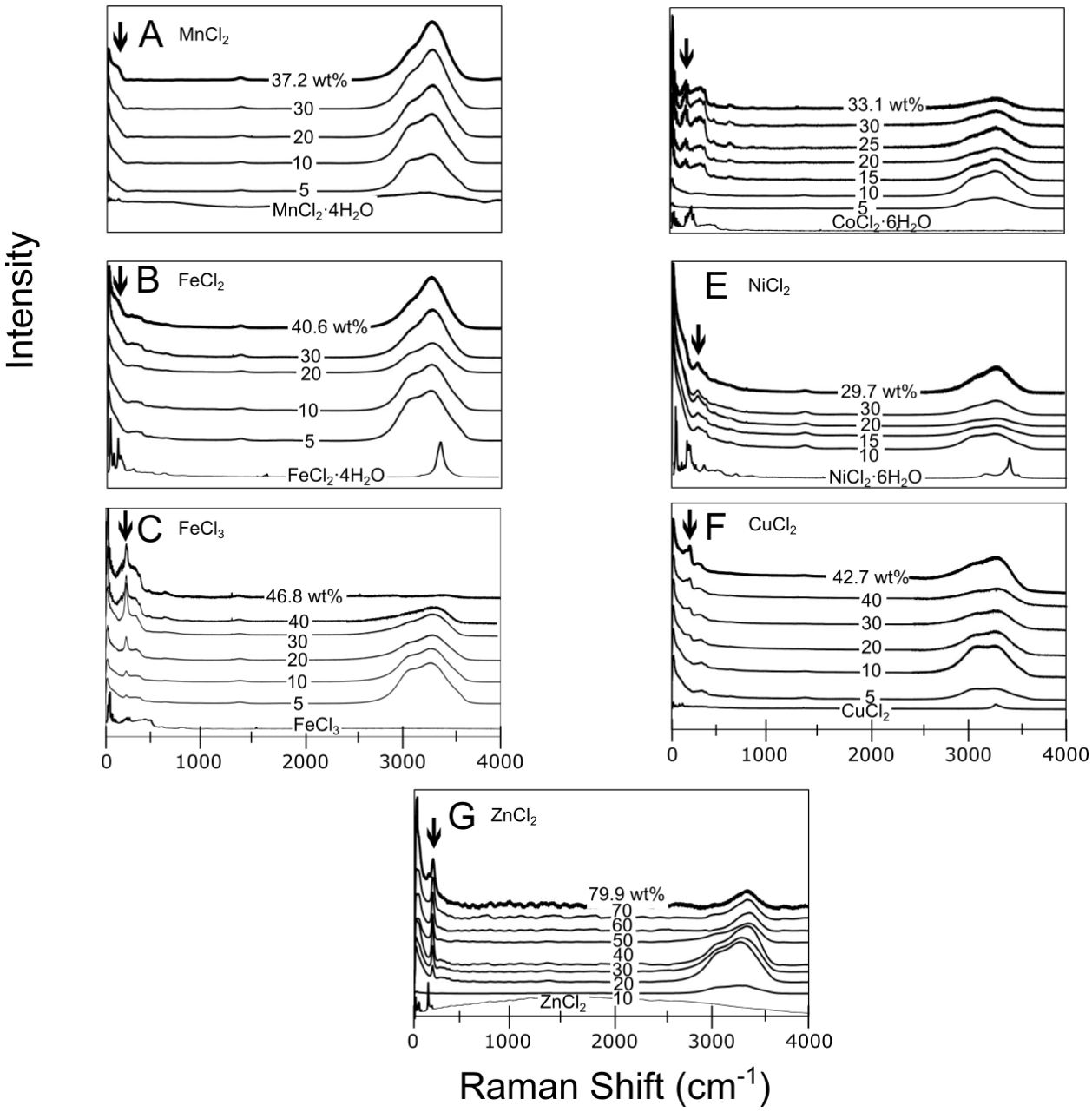

Figure 6. Raman spectra of first row transition metals from 50 to 4000 cm^{-1} A) $MnCl_2$, B) $FeCl_2$, C) $FeCl_3$, D) $CoCl_2$, E) $NiCl_2$, F) $CuCl_2$, G) $ZnCl_2$.

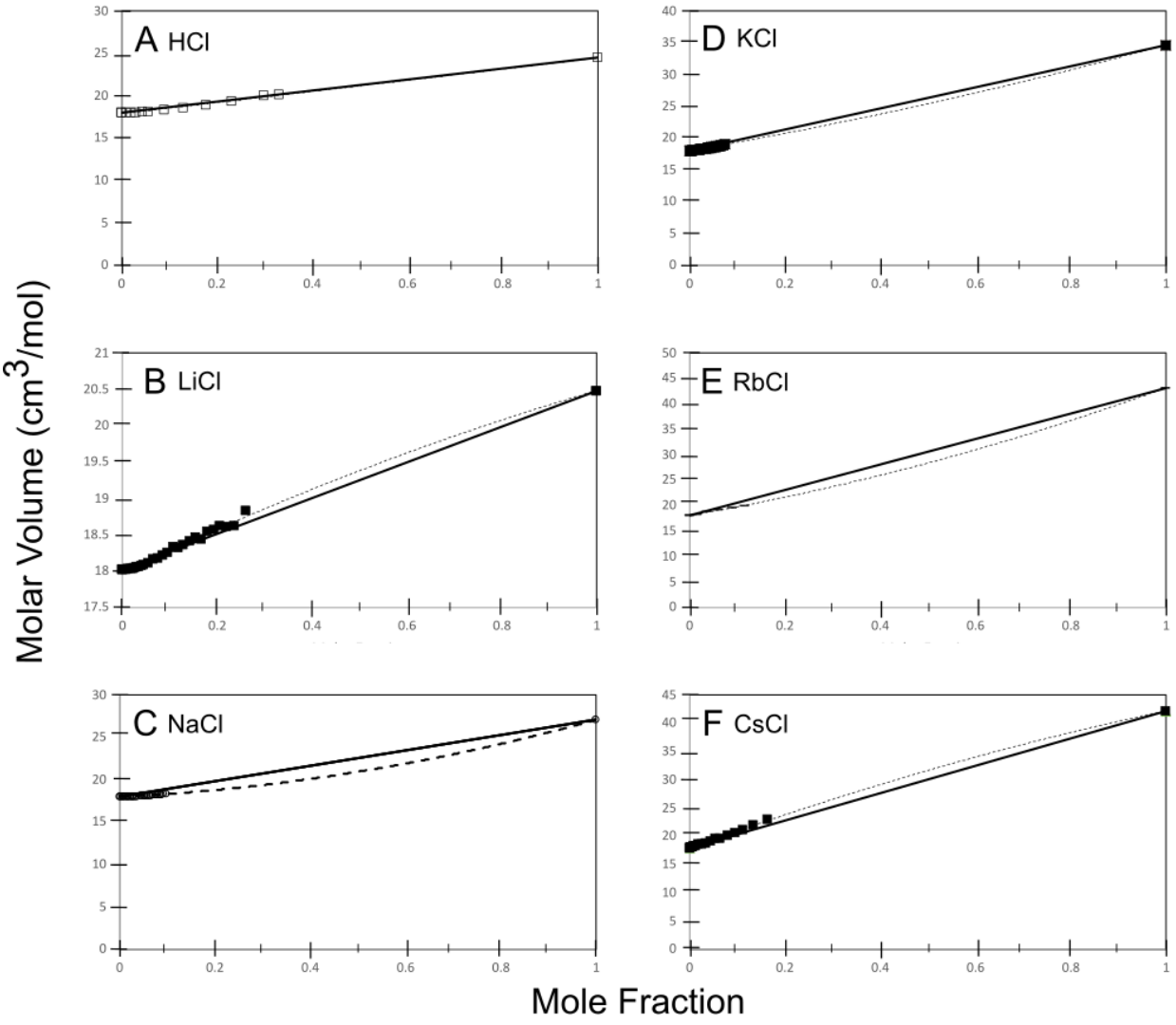

Figure 7. Partial molar volume versus mole fraction concentration. The straight line represents ideal mixing, and the fitted line shows the departure from ideality for alkali chlorides. A) HCl, B) LiCl, C) NaCl, D) KCl, E) RbCl, F) CsCl.

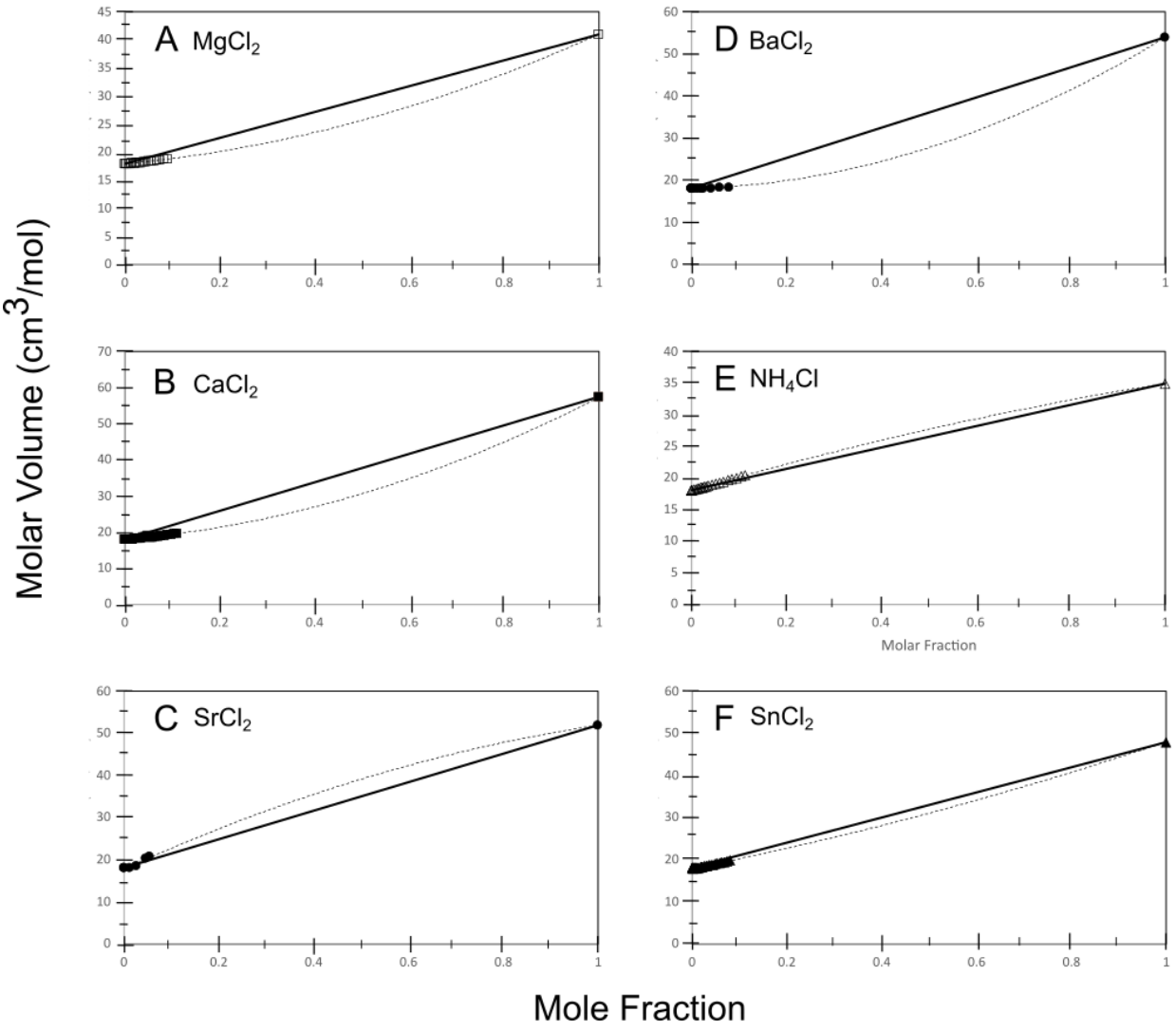

Figure 8. Partial molar volume versus mole fraction concentration. The straight line represents ideal mixing, and the fitted line shows the departure from ideality for alkaline Earth metals, tin(II), and ammonium chlorides. A) $MgCl_2$, B) $CaCl_2$, C) $SrCl_2$, D) $BaCl_2$, E) $SnCl_2$, F) NH_4Cl.

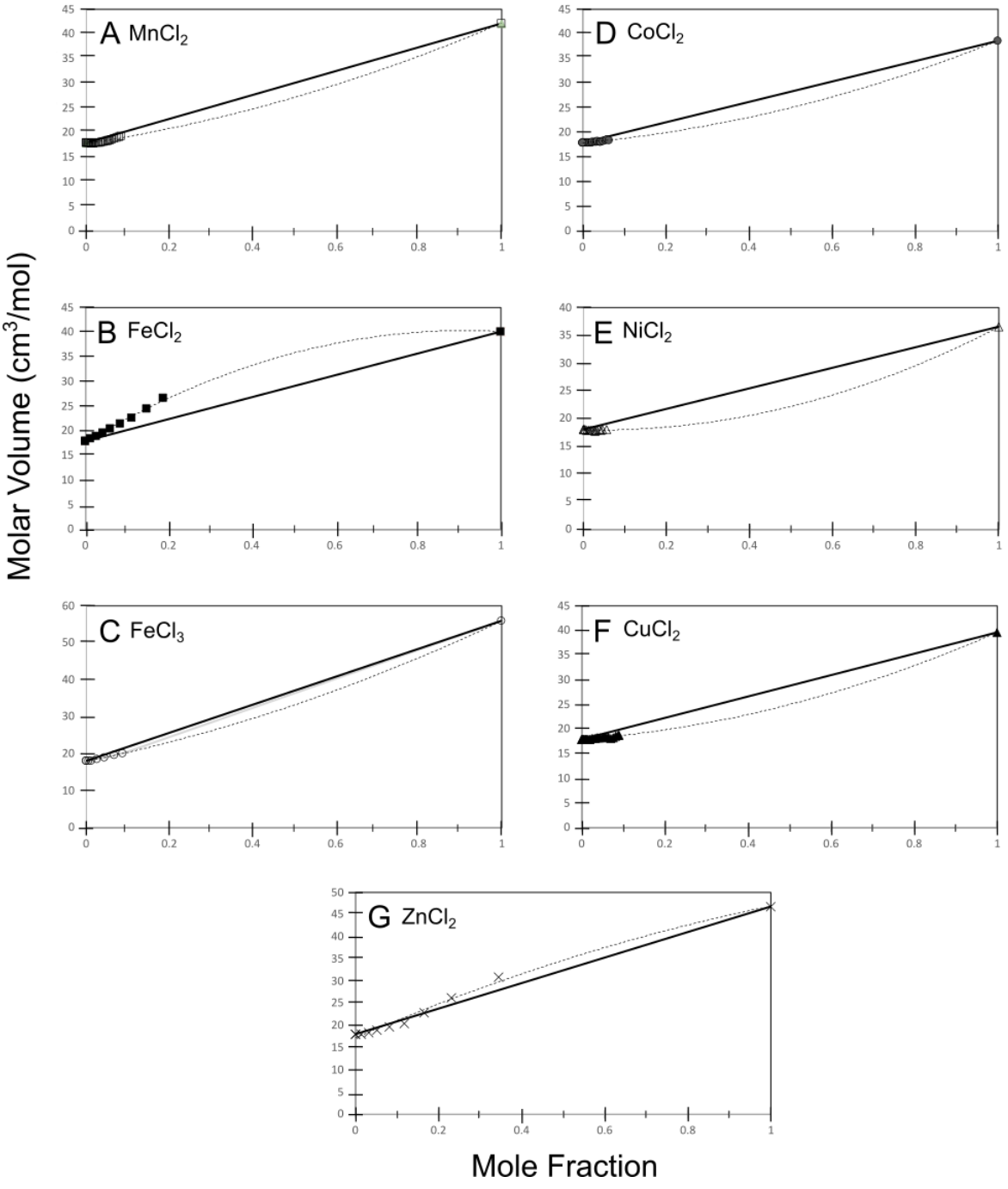

Figure 9. Partial molar volume versus mole fraction concentration. The straight line represents ideal mixing, and the fitted line shows the departure from ideality for first row transition metals. A) $MnCl_2$, B) $FeCl_2$, C) $FeCl_3$, D) $CoCl_2$, E) $NiCl_2$, F) $CuCl_2$, G) $ZnCl_2$.

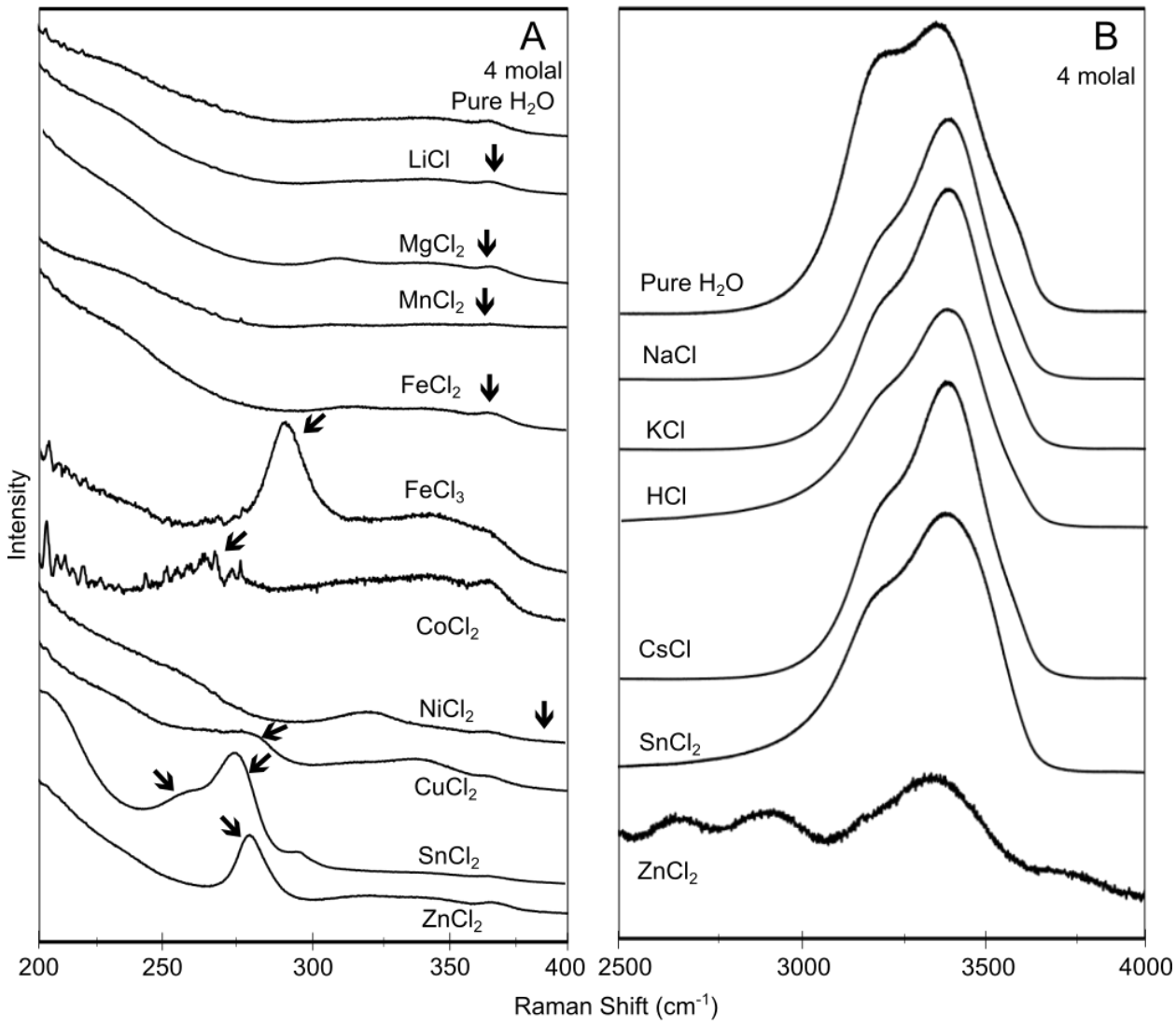

Figure 10. Comparisons of A) Raman shift 200 to 400 cm^{-1} and B) OH-stretching region of various chloride solutes at 4 molal concentration.

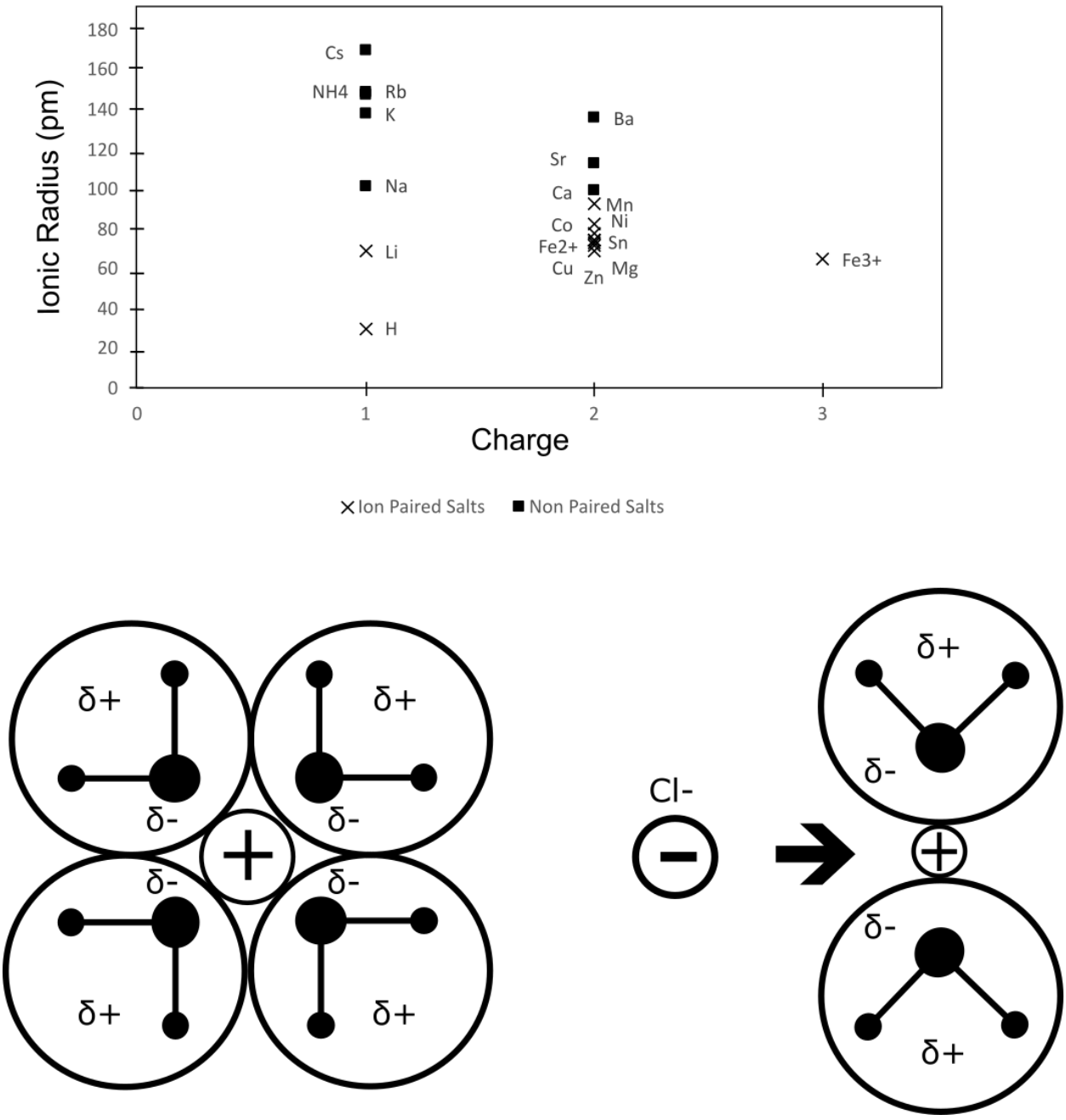

Figure 11. A) Charge versus ionic radius for cations analyzed in this study, grouped according to whether or not the chloride salt shows evidence of ion pairing. Ionic radii from Marcus (1991). B) Schematic diagram illustrating a simple, conceptual model for why smaller cations show evidence of ion pairing.

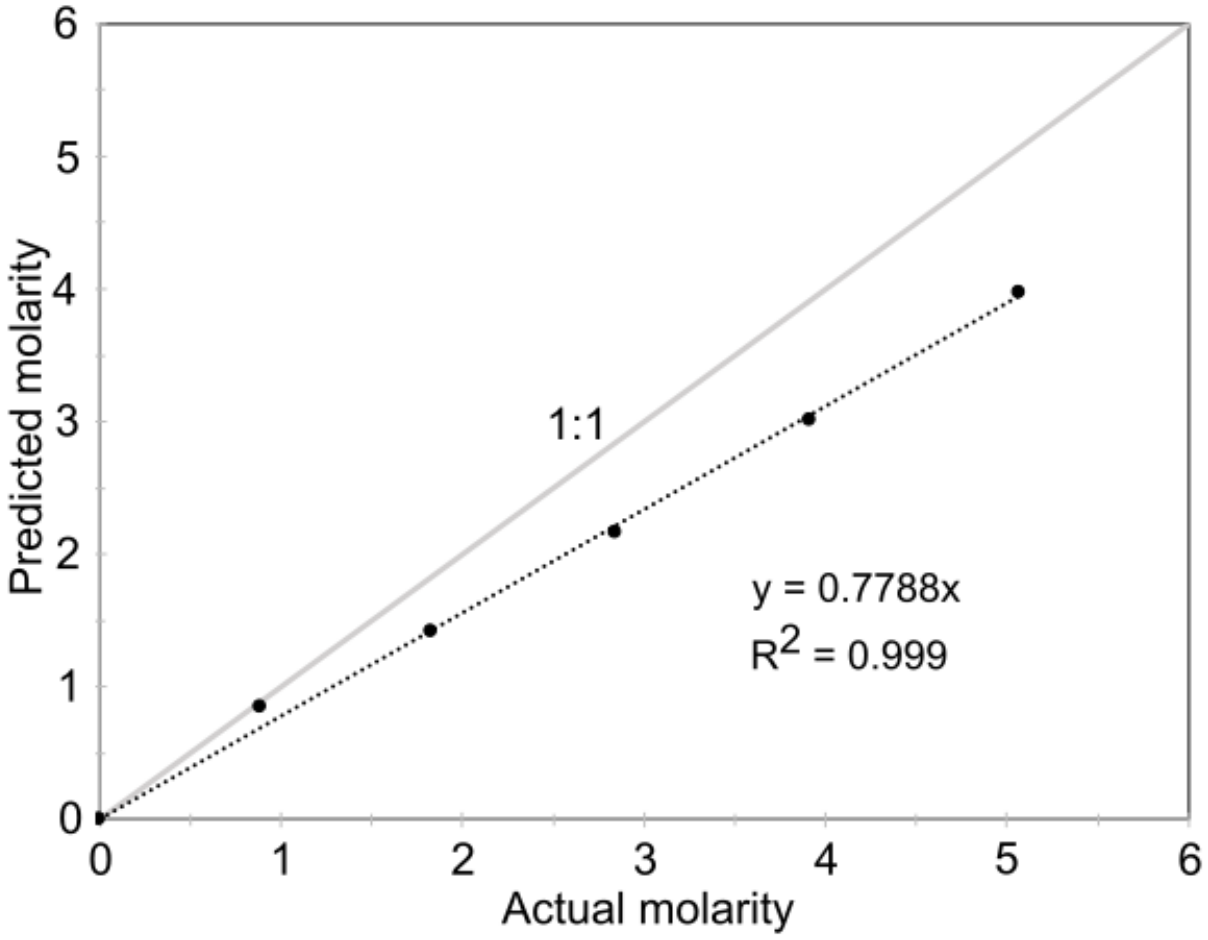

Figure 12. Comparison of actual versus calculated chloride molarity using the equation of Sun et al. (2010), showing an excellent linear correlation, but systematic underestimation of actual chloride molarity, which probably reflects differences between individual Raman instruments.

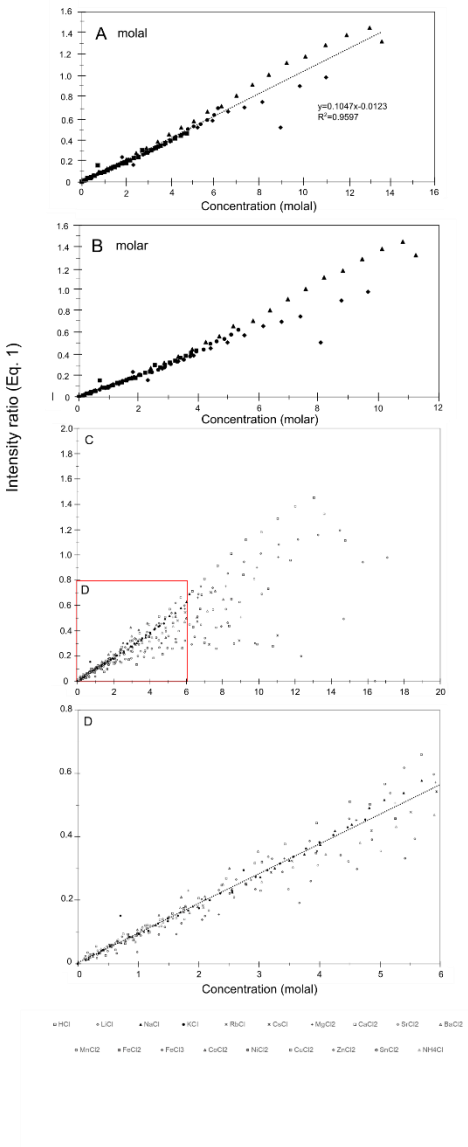

Figure 13. A) Molal concentration (moles Cl per kg H_2O) chloride in NaCl, KCl, $CaCl_2$, and $MgCl_2$ solutions versus peak intensity ratio as per Eq. (1). B) The same data as in A, but transformed to the molar concentration scale (moles Cl per litre of solution). Note that the molal scale in panel A yields a somewhat better fit compared to the molar scale in B. C) Molal concentration of chloride in solution for all solutes from this study up to 20 molal versus peak intensity ratio as per Eq. (1). D) Close-up view of the same data as in panel C, up to 6 molal Cl for most salts (except $CoCl_2$ > 2.5 molal, $CuCl_2$ > 1.1 molal, and $SnCl_2$ > 1.4 molal).

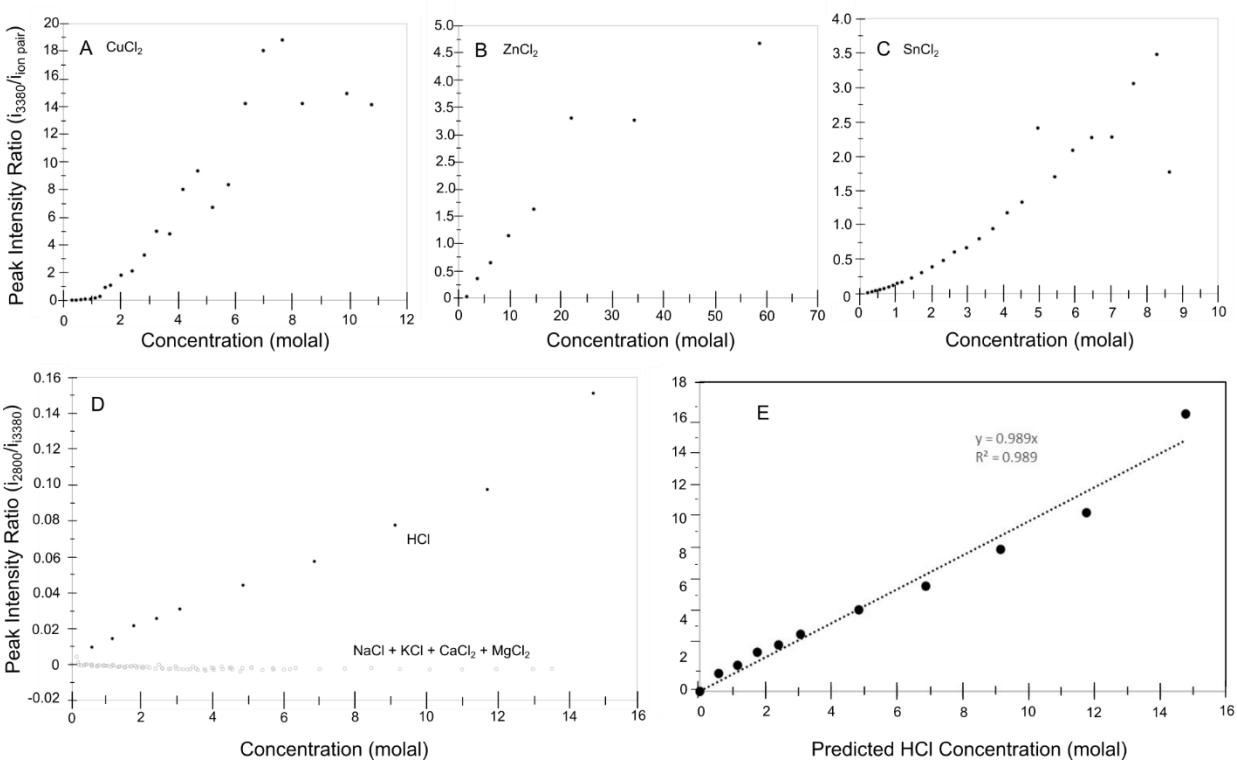

Figure 14. A-C: Correlations of the peak intensity ratio for the ion pair as per Eq. (2) with molal concentration of chloride for A) $CuCl_2$ B) $ZnCl_2$ and C) $SnCl_2$ D) Correlation of the peak intensity ratio as per Eq. (3) with molal concentration of HCl. Note that for the neutral salts NaCl, KCl, $MgCl_2$ and $CaCl_2$, the ratio as per Eq. (3) is zero independently of concentration. E) Comparison of the HCl concentration in our $SnCl_2$ solutions as calculated according to Eq. (3), with the known (measured) concentration.

REFERENCES

Agmon, N. (1998). Structure of Concentrated HCl Solutions. *The Journal of Physical Chemistry A*, *102*(1), 192–199. https://doi.org/10.1021/jp970836x

Agulló-Rueda, F., Calleja, J. M., Martini, M., Spinolo, G., & Cariati, F. (1987). Raman and infrared spectra of transition metal halide hexahydrates. *Journal of Raman spectroscopy*, *18*(7), 485-491.

Alsayoud, A. Q., Venkateswara Rao, M., Edwards, A. N., Deymier, P. A., Muralidharan, K., Potter Jr, B. G., ... & Lucas, P. (2016). Structure of ZnCl2 melt. Part I: Raman spectroscopy analysis driven by ab initio methods. *The Journal of Physical Chemistry B*, *120*(17), 4174-4181

Ananthanarayanan, V. (1970). Force Constants of Octahedral M (H2O) 6 Complexes: M= Mg, Zn, Ni, or Al. *The Journal of Chemical Physics*, *52*(7), 3844-3845.

Audétat, A. (2019) The Metal Content of Magmatic-Hydrothermal Fluids and Its Relationship to Mineralization Potential. Economic Geology, 14(6), 1033–1056. https://doi.org/10.5382/econgeo.4673

Ault, B. S., & Andrews, L. (1976). Infrared and Raman spectra of the $M^+Cl_3^-$ ion pairs and their chlorine–bromine counterparts isolated in argon matrices. *The Journal of Chemical Physics*, *64*(12), 4853–4859. https://doi.org/10.1063/1.432141

Bach R. D., Shobe D. S., Schlegel H. B. & Nagel C. J. (1996) Thermochemistry of iron chlorides and their positive and negative ions. Journal of Physical Chemistry, 100, 8770–8776. https://doi.org/ 10.1021/jp953687w.

Balasubrahmanyam, K. (1966) Raman Spectra of Liquid MgCl2 and Liquid MgCl2–KCl System. Journal of Chemical Physics, 44, 3270. https://doi.org/10.1063/1.1727223

Baumgartner, M., & Bakker, R. J. (2009). Raman spectroscopy of pure H_2O and NaCl-H_2O containing synthetic fluid inclusions in quartz—A study of polarization effects. *Mineralogy and Petrology*, *95*(1–2), 1–15. https://doi.org/10.1007/s00710-008-0028-z

Bodnar, R. J., Lecumberri-Sanchez, P., Moncada, D., & Steele-MacInnis, M. (2014). Fluid Inclusions in Hydrothermal Ore Deposits. In *Treatise on Geochemistry* (pp. 119–142). Elsevier. https://doi.org/10.1016/B978-0-08-095975-7.01105-0

Bodnar, R.J. & Frezzotti, M.L. (2020) Microscale chemistry: Raman analysis of fluid and melt inclusions. *Elements*, 16(2), 93-98. https://doi.org/10.2138/gselements.16.2.93

Borisova, A.Y., Thomas, R., Salvi, S., Candaudap, F., Lanzazona, A., Chmeleff, J. (2012) Tin and associated metal and metalloid geochemistry by femtosecond LA-ICP-QMS microanalysis of pegmatite–leucogranite melt and fluid inclusions: new evidence for melt–melt–fluid immiscibility. Mineralogical Magazine, 76 (1): 91–113. https://doi.org/10.1180/minmag.2012.076.1.91

Brewer, L., Somayajulu, G.R., & Brackett E. (1963) Thermodynamic Properties of Gaseous Metal Dihalides. *Chemical Reviews*, 63, 111–121. https://doi.org/10.1021/cr60222a002

Brooks, H.L., Steele-MacInnis, M. (2019) A model for the solubility of minerals in saline aqueous fluids in the crust and upper mantle. *American Journal of Science*, 319, 754-787. doi:10.2475/09.2019.02

Burke, E.A. (2001) Raman microspectrometry of fluid inclusions. *Lithos*, 55, 139-158. https://doi.org/10.1016/S0024-4937(00)00043-8

Busing, W. R., & Hornig, D. F. (1961). THE EFFECT OF DISSOLVED KBr, KOH OR HCl ON THE RAMAN SPECTRUM OF WATER. *The Journal of Physical Chemistry*, *65*(2), 284-292.

Brubach J.-B., Mermet A., Filabozzi A., Gerschel A. & Roy P. (2005) Signatures of the hydrogen bonding in the infrared bands of water. J. Chem. Phys. 122, 184509.

Carey, D. M., & Korenowski, G. M. (1998). Measurement of the Raman spectrum of liquid water. *The Journal of Chemical Physics*, *108*(7), 2669–2675. https://doi.org/10.1063/1.475659

Chou, I. M. (2012). Optical cells with fused silica windows for the study of geological fluids. In: J. Dubessy, M.-C. Caumon, F. Rull (eds.): *Applications of Raman Spectroscopy to Earth Sciences and Cultural Heritage*. European Mineralogical Union, Notes in Mineralogy v. 12, pp. 227-248.

Chumaevskii, N. A., Rodnikova, M. N., & Sirotkin, D.A. (2001). Cationic effect in aqueous solutions of 1:1 electrolytes by Raman spectral data. *Journal of Molecular Liquids*, 91, 81-90. https://doi.org/10.1016/S0167-7322(01)00148-9

Collins, K. D. (1997). Charge density-dependent strength of hydration and biological structure. *Biophysical Journal*, *72*(1), 65-76. https://doi.org/10.1016/S0006-3495(97)78647-8

Collins, K.D. (2006) Ion hydration: Implications for cellular function, polyelectrolytes, and protein crystallization. Biophysical Chemistry, 119(3), 271-281. https://doi.org/10.1016/j.bpc.2005.08.010

Davey, J., Roberts, S., Wilkinson, J.J. (2021) Copper- and cobalt-rich, ultrapotassic bittern brines responsible for the formation of the Nkana-Mindola deposits, Zambian Copperbelt. Geology, 49(3), 341–345. https://doi.org/10.1130/G48176.1

Devendorf, G. S., Ben-Amotz, D., & de Souza, L. E. S. (1996). Raman spectroscopy and theoretical modeling of HCl vibrational frequency shifts in high pressure argon. *The Journal of Chemical Physics*, *104*(10), 3479–3485. https://doi.org/10.1063/1.471053

DeVitre, C. L., Allison, C. M., & Gazel, E. (2021). A high-precision CO2 densimeter for Raman spectroscopy using a Fluid Density Calibration Apparatus. *Chemical Geology*, *584*, 120522.

Dubessy, J., Boiron, M. C., Moissette, A., Monnin, C., & Sretenskaya, N. (1992). Determinations of water, hydrates and pH in fluid inclusions by micro-Raman spectrometry. *European Journal of Mineralogy*, 885-894.

Eigen, M., & Tamm, K. (1962). Schallabsorption in elektrolytlösungen als folge chemischer relaxation I. Relaxationstheorie der mehrstufigen dissoziation. *Zeitschrift für Elektrochemie, Berichte der Bunsengesellschaft für physikalische Chemie*, *66*(2), 93-107.

Foustoukos, D.I. (2016) On the solvation properties of supercritical electrolyte solutions. Chemical Geology, 447, 191-198. https://doi.org/10.1016/j.chemgeo.2016.10.039

Frezzotti, M. L., Tecce, F., & Casagli, A. (2012). Raman spectroscopy for fluid inclusion analysis. *Journal of Geochemical Exploration*, *112*, 1–20. https://doi.org/10.1016/j.gexplo.2011.09.009

Furic, K., & Ciglenečki, I., Ćosović, B. (2000). Raman spectroscopic study of sodium chloride water solutions. *Journal of Molecular Structure*, 550-551, 225-234. https://doi.org/10.1016/S0022-2860(00)00388-4

Garcia-Baonza, V., Rull, F., & Dubessy, J. (2012). Raman spectroscopy of gases, water and other geological fluids. In: J. Dubessy, M.-C. Caumon, F. Rull (eds.): *Applications of Raman Spectroscopy to Earth Sciences and Cultural Heritage*. European Mineralogical Union, Notes in Mineralogy v. 12, pp. 279-320.

Grayson, M. (2005). The Infrared and Raman Spectroscopic Signals of HF, HCl, HBr and HI. *Internet Electronic Journal of Molecular Design*, 4, 786-792.

Huang, C. H., & Brooker, M. H. (1976). Raman spectrum of molten MgCl2. *Chemical Physics Letters*, *43*(1), 180-182.

Irish, D. E., McCarroll, B., & Young, T. F. (1963). Raman study of zinc chloride solutions. *The Journal of Chemical Physics*, *39*(12), 3436-3444.

Irish, D. E., (1967). Raman Spectroscopy of Complex Ions in Solution. In: H.A. Szymanski (ed.), *Raman Spectroscopy: Theory and Practice*. pp. 224-250.

Kanno H. & Hiraishi J. (1982) A Raman study of aqueous solutions of ferric nitrate, ferrous chloride and ferric chloride in the glassy state. Journal of Raman Spectrosccopy, 12, 224–227. https://doi. org/10.1002/jrs.1250120305.

Khoshtariya, D. E., Zahl, A., Dolidze, T. D., Neubrand, A., & van Eldik, R. (2004). Discrimination of Diverse (Pressure/Temperature-Dependent/Independent) Inherent Sub-structures in Liquid Water (D_2O) from Difference Vibrational Spectroscopy. *The Journal of Physical Chemistry B*, *108*(39), 14796–14799. https://doi.org/10.1021/jp047333t

Klyukin, Yu.I., Driesner, T., Steele-MacInnis, M., Bodnar, R.J. (2016) Effect of salinity on mass and energy transport by hydrothermal fluids in the critical region based on the physical and thermodynamic properties of H_2O-NaCl. *Geofluids* 16, 585-603. doi: 10.1111/gfl.12181

Krishnan, R.S. (1947) Raman spectrum of ammonium chloride and its variation with temperature. *Proceedings of the Indian Academy of Science,* 26, 432-449. https://doi.org/10.1007/BF03170900

Lamadrid, H. M., Moore, L. R., Moncada, D., Rimstidt, J. D., Burruss, R. C., & Bodnar, R. J. (2017). Reassessment of the Raman CO_2 densimeter. *Chemical Geology*, *450*, 210–222. https://doi.org/10.1016/j.chemgeo.2016.12.034

Lamadrid, H., Steele-MacInnis, M., Bodnar, R.J. (2018) Relationship between Raman spectral features and fugacity in mixtures of gases. *Journal of Raman Spectroscopy*, 49, 581-593. doi:10.1002/jrs.5304

Lecumberri-Sanchez, P., Steele-MacInnis, M. & Bodnar, R.J. (2015) Synthetic fluid inclusions XIX. Experimental determination of the vapor-saturated liquidus of the system H_2O-NaCl-$FeCl_2$. *Geochimica et Cosmochimica Acta* 148, 34-49. doi:10.1016/j.gca.2014.08.015

Li F., Li S., Zhuang X., & Yuan J. (2017). Study on the structure of potassium chloride aqueous solution by molecular dynamics and Raman spectroscopy methods. *Chemical Engineering Transactions*, *61*, 769–774. https://doi.org/10.3303/CET1761126

Lin, F., Bodnar, R.J. & Becker, S.P. (2007) Experimental determination of the Raman CH_4 symmetric stretching ($\nu 1$) band position from 1–650 bar and 0.3–22 °C: Application to

fluid inclusion studies. Geochimica et Cosmochimica Acta, 71, 3746-3756. https://doi.org/10.1016/j.gca.2007.05.016

Lund, M., Jagoda-Cwiklik, B., Woodward, C. E., Vácha, R., & Jungwirth, P. (2010). Dielectric interpretation of specificity of ion pairing in water. *The Journal of Physical Chemistry Letters*, *1*(1), 300-303.

Marcus, Y. (1991). Thermodynamics of Solvation of Ions: Part 5. Gibbs free energy of hydration at 298.15 K. *Journal of the Chemical Society, Faraday Transactions.*, *87*(18), 2995-2999.

Marcus, Y. (2005). Electrostriction, ion solvation, and solvent release on ion pairing. *The Journal of Physical Chemistry B*, *109*(39), 18541-18549.

Marcus, Y., & Hefter, G. (2006). Ion Pairing. *Chemical Reviews*, *106*(11), 4585–4621. https://doi.org/10.1021/cr040087x

Medeiros, F. E. O., Araújo, B. S., & Ayala, A. P. (2018). Raman spectroscopy investigation of the thermal stability of the multiferroic $CuCl_2$ and its hydrated form. *Vibrational Spectroscopy*, *99*, 1-6.

Mercadier, J., Richard, A., & Cathelineau, M. (2012) Boron- and magnesium-rich marine brines at the origin of giant unconformity-related uranium deposits: δ11B evidence from Mg-tourmalines. *Geology*, 40(3), 231-234. https://doi.org/10.1130/G32509.1

Mernagh, T. P., & Wilde, A. R. (1989). The use of the laser Raman microprobe for the determination of salinity in fluid inclusions. *Geochimica et Cosmochimica Acta*, *53*(4), 765–771. https://doi.org/10.1016/0016-7037(89)90022-7

Pauling, L. (1929) The principles determining the structure of complex ionic crystals. *Journal of the American Chemical Society,* 51(4), 1010–1026. https://doi.org/10.1021/ja01379a006

Pereira, S. I., Diehl, A., McDermott, J. M., Pape, T., Klose, L., Strauss, H., Bohrmann, G., & Bach, W. (2022). Geochemistry of Hydrothermal Fluids From the E2-Segment of the East Scotia Ridge: Magmatic Input, Reaction Zone Processes, Fluid Mixing Regimes and Bioenergetic Landscapes. *Frontiers in Marine Science*, *9*, 765648. https://doi.org/10.3389/fmars.2022.765648

Pye, C. C., & Rudolph, W. W. (1998). An ab initio and Raman investigation of magnesium (II) hydration. *The Journal of Physical Chemistry A*, *102*(48), 9933-9943.

Reimer, J., Steele-MacInnis, M., Wambach, J.M., Vogel, F. (2015) Ion association in hydrothermal sodium sulfate solutions studied by modulated FT-IR-Raman spectroscopy and molecular dynamics. Journal of Physical Chemistry B 119, 9847-9857. https://doi.org/10.1021/acs.jpcb.5b03192

Remigi, S., Mancini, T., Ferrando, S., & Frezzotti, M. L. (2021). Interlaboratory Application of Raman CO_2 Densimeter Equations: Experimental Procedure and Statistical Analysis Using Bootstrapped Confidence Intervals. *Applied Spectroscopy*, *75*(7), 867–881. https://doi.org/10.1177/0003702820987601

Richard, A., Banks, D. A., Mercadier, J., Boiron, M. C., Cuney, M., & Cathelineau, M. (2011) An evaporated seawater origin for the ore-forming brines in unconformity-related uranium deposits (Athabasca Basin, Canada): Cl/Br and δ37Cl analysis of fluid inclusions. *Geochimica et Cosmochimica Acta*, 75(10), 2792-2810. https://doi.org/10.1016/j.gca.2011.02.026

Rudolph, W., Brooker, M.H., & Pye, C.C. (1995) Hydration of Lithium Ion in Aqueous Solution. *Journal of Physical Chemistry,* 99, 3793-3797. https://doi.org/10.1021/j100011a055

Salant, E. O., & Sandow, A. (1931). Modified Scattering by Hydrogen Halides. *Physical Review*, *37*(4), 373–378. https://doi.org/10.1103/PhysRev.37.373

Schmidt, C. (2018). Formation of hydrothermal tin deposits: Raman spectroscopic evidence for an important role of aqueous Sn(IV) species. *Geochimica et Cosmochimica Acta*, *220*, 499–511. https://doi.org/10.1016/j.gca.2017.10.011

Schmidt, C. & Chou, I.M. (2012) The hydrothermal diamond anvil cell (HDAC) for Raman spectroscopic studies of geological fluids at high pressures and temperatures. In: J. Dubessy, M.-C. Caumon, F. Rull (eds.): *Applications of Raman Spectroscopy to Earth Sciences and Cultural Heritage*. European Mineralogical Union, Notes in Mineralogy v. 12, pp. 247-276.

Scholten, L., Schmidt, C., Lecumberri-Sanchez, P., Newville, M., Lanzirotti, A., Sirbescu, M.-L.C., Steele-MacInnis, M. (2019) Solubility and speciation of iron in hydrothermal fluids. *Geochimica et Cosmochimica Acta*, 252, 126-143. https://doi.org/10.1016/j.gca.2019.03.001

Schultz, J.W. & Hornig, D.F. (1961) THE EFFECT OF DISSOLVED ALKALI HALIDES ON THE RAMAN SPECTRUM OF WATER. *The Journal of Physical Chemistry*, 65, 2131-2138.

Senanayake, H. S., Greathouse, J. A., Ilgen, A. G., & Thompson, W. H. (2021). Simulations of the IR and Raman spectra of water confined in amorphous silica slit pores. *The Journal of Chemical Physics*, *154*(10), 104503.

Shaffer C. A. (1997) Quantification of Hydroxide in Aqueous Solutions by Raman Spectroscopy. US Department of Energy (DOE), Washington DC, 31 pp.

Spiekermann, G., Steele-MacInnis, M., Kowalski, P., Schmidt, C & Jahn, S. (2012) Vibrational mode frequencies of H4SiO4, D4SiO4, H6Si2O7 and H6Si3O9 in aqueous environment, obtained from ab initio molecular dynamics. *Journal of Chemical Physics* 137, 164506. http://dx.doi.org/10.1063/1.4761824

Srivastava, B.K., Khandelwal, D.P. & Bist, H.D. (1978) Raman scattering and vibrational dynamics of MnCl2·2H2O. Journal of Raman Spectroscopy, 7, 202-204. https://doi.org/10.1002/jrs.1250070408

Steele-MacInnis, M., Lecumberri-Sanchez, P. & Bodnar, R.J. (2015) Synthetic fluid inclusions XX. Critical *PTx* properties of H_2O-$FeCl_2$ fluids. *Geochimica et Cosmochimica Acta* 148, 50-61. https://doi.org/10.1016/j.gca.2014.09.026

Steele-MacInnis, M., Lecumberri-Sanchez, P., Marshall, D., Kontak, D. (2021) Contribution of fluid inclusions to genetic models for ore deposits. In: P. Lecumberri-Sanchez, M. Steele-MacInnis, & D. Kontak (eds.) *Fluid and Melt Inclusions: Applications to Geologic Processes*. Mineralogical Association of Canada short course volume 49, pp. 195-242.

Steele-MacInnis, M., Manning, C.E. (2020) Hydrothermal properties of geologic fluids. *Elements*, 16, 375-380. https://doi.org/10.2138/gselements.16.6.375

Steele-MacInnis, M., Ridley, J., Lecumberri-Sanchez, P., Schlegel, T., Heinrich, C.A. (2016) Application of low-temperature microthermometric data for interpreting multicomponent fluid inclusion compositions. *Earth-Science Reviews* 159, 14-35. https://doi.org/10.1016/j.earscirev.2016.04.011

Steele-MacInnis, M. & Schmidt, C. (2014) Silicate speciation in H_2O–Na_2O–SiO_2 fluids from 3 to 40 mol% SiO_2, to 600 °C and 2 GPa. *Geochimica et Cosmochimica Acta,* 136, 126-141. doi:10.1016/j.gca.2014.04.009

Steinbach, C., Andersson, P., Kazimirski, J. K., Buck, U., Buch, V., & Beu, T. A. (2004). Infrared Predissociation Spectroscopy of Large Water Clusters: A Unique Probe of Cluster Surfaces. *The Journal of Physical Chemistry A*, *108*(29), 6165–6174. https://doi.org/10.1021/jp049276+

Sublett, D.M., Sendula, E., Lamadrid, H., Steele-MacInnis, M., Spiekermann, G., Burruss, R.C., Bodnar, R.J. (2021) Raman spectral behavior of N2, CO2 and CH4 in N2-CO2-CH4 gas mixtures from 22-200°C and 10-500 bars. *Journal of Raman Spectroscopy*, 52, 750-769. https://doi.org/10.1002/jrs.6033

Suffren, Y., Rollet, F. G., & Reber, C. (2011). Raman spectroscopy of transition metal complexes: molecular vibrational frequencies, phase transitions, isomers, and electronic structure. *Comments on Inorganic Chemistry*, *32*(5-6), 246-276.

Sun, Q. (2009). The Raman OH stretching bands of liquid water. *Vibrational Spectroscopy*, *51*(2), 213–217. https://doi.org/10.1016/j.vibspec.2009.05.002

Sun, Q., Zhao, L., Li, N., & Liu, J. (2010). Raman spectroscopic study for the determination of Cl^- concentration (molarity scale) in aqueous solutions: Application to fluid inclusions. *Chemical Geology*, *272*(1–4), 55–61. https://doi.org/10.1016/j.chemgeo.2010.02.004

Szmihelsky, M., Steele-MacInnis, M., Bain, W.M., Falck, H., Adair, R., Campbell, B., Dufrane, S.A., Went, A. & Corlett, H.J. (2021) Mixing brine with oil triggered sphalerite

deposition at Pine Point, Northwest Territories, Canada. *Geology*, 49, 488-492. https://doi.org/10.1130/G48259.1

Van Daele, Hulsbosch, N., Dewaele, S., Boiron, M.-C., Piessens, K., Boyce, A. Muchez, Ph. (2018) Mixing of magmatic-hydrothermal and metamorphic fluids and the origin of peribatholitic Sn vein-type deposits in Rwanda. Ore Geology Reviews, 101, 481-501. https://doi.org/10.1016/j.oregeorev.2018.07.020

Walrafen, G.E. (1962) Raman Spectral Studies of the Effects of Electrolytes on Water. Journal of Chemical Physics, 36, 1035. https://doi.org/10.1063/1.1732628

Walrafen, G. E., & Chu, Y. C. (1995). Linearity between structural correlation length and correlated-proton Raman intensity from amorphous ice and supercooled water up to dense supercritical steam. *The Journal of Physical Chemistry*, *99*(28), 11225–11229. https://doi.org/10.1021/j100028a025

Walter, B., Steele-MacInnis, M., Markl, G. (2017) Sulfate brines in fluid inclusions of hydrothermal veins: Compositional determinations in the system H_2O-Na-Ca-Cl-SO_4. Geochimica et Cosmochimica Acta 209, 184-203. https://doi.org/10.1016/j.gca.2017.04.027

Yardley, B. W. (2005). 100th Anniversary Special Paper: metal concentrations in crustal fluids and their relationship to ore formation. *Economic Geology*, *100*(4), 613-632.